

First HETDEX Spectroscopic Determinations of Ly α and UV Luminosity Functions at $z = 2 - 3$: Bridging a Gap Between Faint AGN and Bright Galaxies

YECHI ZHANG,^{1,2} MASAMI OUCHI,^{3,1,4} KARL GEBHARDT,⁵ ERIN MENTUCH COOPER,⁵ CHENXU LIU,⁵ DUSTIN DAVIS,⁵
DONGHUI JEONG,^{6,7} DANIEL J. FARROW,^{8,9} STEVEN L. FINKELSTEIN,⁵ ERIC GAWISER,¹⁰ GARY J. HILL,^{11,5}
YUICHI HARIKANE,^{1,12} RYOTA KAKUMA,¹ VIVIANA ACQUAVIVA,^{13,14} CAITLIN M. CASEY,⁵ MAXIMILIAN FABRICIUS,^{8,9}
ULRICH HOPP,^{8,9} MATT J. JARVIS,^{15,16} MARTIN LANDRIAU,¹⁷ KEN MAWATARI,^{1,3} SHIRO MUKAE,¹ YOSHIAKI ONO,¹
NAO SAKAI,¹ AND DONALD P. SCHNEIDER^{6,7}

¹*Institute for Cosmic Ray Research, The University of Tokyo, 5-1-5 Kashiwanoha, Kashiwa, Chiba 277-8582, Japan*

²*Department of Astronomy, Graduate School of Science, the University of Tokyo, 7-3-1 Hongo, Bunkyo, Tokyo 113-0033, Japan*

³*National Astronomical Observatory of Japan, 2-21-1 Osawa, Mitaka, Tokyo 181-8588, Japan*

⁴*Kavli Institute for the Physics and Mathematics of the Universe (Kavli IPMU, WPI), The University of Tokyo, 5-1-5 Kashiwanoha, Kashiwa, Chiba, 277-8583, Japan*

⁵*Department of Astronomy, The University of Texas at Austin, 2515 Speedway, Stop C1400, Austin, Texas 78712, USA*

⁶*Department of Astronomy and Astrophysics, The Pennsylvania State University, University Park, PA 16802, USA*

⁷*Institute for Gravitation and the Cosmos, The Pennsylvania State University, University Park, PA 16802, USA*

⁸*Max-Planck Institut für extraterrestrische Physik, Giessenbachstrasse 1, 85748 Garching, Germany*

⁹*University Observatory, Fakultät für Physik, Ludwig-Maximilians University Munich, Scheiner Strasse 1, 81679 Munich, Germany*

¹⁰*Department of Physics and Astronomy, Rutgers, The State University of New Jersey, Piscataway, NJ 08854, USA*

¹¹*McDonald Observatory, University of Texas at Austin, 2515 Speedway, Stop C1402, Austin, TX 78712, USA*

¹²*Department of Physics and Astronomy, University College London, Gower Street, London WC1E 6BT, UK*

¹³*Physics Department, NYC College of Technology, 300 Jay Street, Brooklyn, NY 11201, USA*

¹⁴*Center for Computational Astrophysics, Flatiron Institute, New York, NY 10010, USA*

¹⁵*Astrophysics, Department of Physics, Keble Road, Oxford, OX1 3RH, UK*

¹⁶*Department of Physics & Astronomy, University of the WesternCape, Private Bag X17, Bellville, Cape Town, 7535, South Africa*

¹⁷*Lawrence Berkeley National Laboratory, 1 Cyclotron Road, Berkeley, CA 94720, USA*

ABSTRACT

We present Ly α and ultraviolet-continuum (UV) luminosity functions (LFs) of galaxies and active galactic nuclei (AGN) at $z = 2.0 - 3.5$ determined by the un-targetted optical spectroscopic survey of the Hobby-Eberly Telescope Dark Energy Experiment (HETDEX). We combine deep Subaru imaging with HETDEX spectra resulting in 11.4 deg² of fiber-spectra sky coverage, obtaining 18320 galaxies spectroscopically identified with Ly α emission, 2126 of which host type 1 AGN showing broad (FWHM > 1000 km s⁻¹) Ly α emission lines. We derive the Ly α (UV) LF over 2 orders of magnitude covering bright galaxies and AGN in $\log L_{\text{Ly}\alpha}/[\text{erg s}^{-1}] = 43.3 - 45.5$ ($-27 < M_{\text{UV}} < -20$) by the $1/V_{\text{max}}$ estimator. Our results reveal the bright-end hump of the Ly α LF is composed of type 1 AGN. In conjunction with previous spectroscopic results at the faint end, we measure a slope of the best-fit Schechter function to be $\alpha_{\text{Sch}} = -1.70_{-0.14}^{+0.13}$, which indicates α_{Sch} steepens from $z = 2 - 3$ towards high redshift. Our UV LF agrees well with previous AGN UV LFs, and extends to faint-AGN and bright-galaxy regimes. The number fraction of Ly α -emitting objects (X_{LAE}) increases from $M_{\text{UV}}^* \sim -21$ to bright magnitude due to the contribution of type 1 AGN, while previous studies claim that $X_{\text{Ly}\alpha}$ decreases from faint magnitude to M_{UV}^* , suggesting a valley in the $X_{\text{Ly}\alpha}$ -magnitude relation at M_{UV}^* . Comparing our UV LF of type 1 AGN at $z = 2 - 3$ with those at $z = 0$, we find that the number density of faint ($M_{\text{UV}} > -21$) type 1 AGN increases from $z \sim 2$ to $z \sim 0$ as opposed to the evolution of bright ($M_{\text{UV}} < -21$) type 1 AGN, suggesting AGN downsizing in the rest-frame UV luminosity.

Keywords: galaxies: formation — galaxies: evolution — galaxies: high-redshift

1. INTRODUCTION

At high redshift, Lyman α emitters (LAEs) are a widely studied population of objects that feature strong Lyman α ($\text{Ly}\alpha$ $\lambda 1216$ Å) emission lines (e.g., Rhoads et al. 2000; Gronwall et al. 2007; Pentericci et al. 2009; Ouchi et al. 2020). Typical LAEs are interpreted as young ($\lesssim 50$ Myr), low-mass ($\lesssim 10^{10} M_{\odot}$) galaxies with high star formation rates (SFR) of $\sim 1 - 100 M_{\odot} \text{ yr}^{-1}$ (e.g., Nagao et al. 2005; Gawiser et al. 2006; Finkelstein et al. 2007, 2008, 2009; Ono et al. 2010a,b; Kashikawa et al. 2012; Harikane et al. 2018). Such properties make LAEs important tracers for galaxy formation at the low-mass end of the spectrum in the early universe, complementary to the continuum selected Lyman Break Galaxies (LBGs) that are relatively massive.

A key statistical property of LAEs is the luminosity function (LF), which is defined as the number density as a function of luminosity. The LAE LFs and their evolution can provide valuable insights into the evolution of young, star forming (SF) galaxies over the cosmic time. Over the past decades, LAEs have been identified and studied with LFs over the redshift range $z \sim 0 - 9$ using deep narrow band (e.g., Gronwall et al. 2007; Ouchi et al. 2008, 2010; Konno et al. 2016, 2018; Tilvi et al. 2020) and spectroscopic surveys (e.g., Blanc et al. 2011; Cassata et al. 2011; Zheng et al. 2013; Drake et al. 2017; Herenz et al. 2019). These studies have found that at $\text{Ly}\alpha$ luminosity $L_{\text{Ly}\alpha} \lesssim 10^{43} \text{ erg s}^{-1}$, the $\text{Ly}\alpha$ LF of LAEs can be described by the Schechter function (Schechter 1976),

$$\phi_{\text{Sch}}(L) d\log L = \ln 10 \phi_{\text{Sch}}^* \left(\frac{L}{L_{\text{Sch}}^*} \right)^{\alpha_{\text{Sch}}+1} \exp \left(-\frac{L}{L_{\text{Sch}}^*} \right) d\log L. \quad (1)$$

The values of L_{Sch}^* , α_{Sch} , and ϕ_{Sch}^* represent the characteristic luminosity, the faint end slope, and the characteristic number density, respectively. Comparing $\text{Ly}\alpha$ LFs at different epochs also shows the redshift evolution of LAEs. From $z \sim 0$ to $z \sim 3$, the number density of LAEs increases rapidly (e.g., Deharveng et al. 2008). At $z \sim 3 - 6$, there is little evolution in the number density of LAEs (e.g., Dawson et al. 2004; Ouchi et al. 2008). Beyond $z \sim 6$, the observed number density of LAEs begins to decrease due to the resonant scattering of $\text{Ly}\alpha$ photon by the increasing neutral hydrogen (HI) fraction in the intergalactic medium (IGM) towards the epoch of reionization (e.g., Kashikawa et al. 2006; Hu et al. 2010; Itoh et al. 2018), although there is also evidence

suggesting no evolution of $\text{Ly}\alpha$ LF from $z = 5.7 - 6.5$ (e.g., Malhotra & Rhoads 2004).

Despite the efforts of previous studies of the $\text{Ly}\alpha$ LFs, several open questions still remain. One open question is the steepness of the faint-end slope of the $\text{Ly}\alpha$ LFs that describes the fraction of faint galaxies relative to brighter ones. Theoretical models of hierarchical structure formation predict that low-mass galaxies are more dominant at higher redshift, which results in a steeper faint-end slope. Such a redshift evolution of the faint-end slope has been identified in the UV continuum LF (hereafter UV LF) of LBGs (e.g., Bouwens et al. 2015; Finkelstein et al. 2015). Since the dust attenuation of $\text{Ly}\alpha$ emission in the interstellar medium (ISM) becomes larger towards fainter UV luminosity (e.g., Ando et al. 2006; Ouchi et al. 2008) and higher redshift (e.g., Blanc et al. 2011; Hayes et al. 2011), the observed faint-end slope of $\text{Ly}\alpha$ LF is expected to be steeper than that of UV LF towards higher redshift. However, the faint-end slope of the $\text{Ly}\alpha$ LF is poorly constrained in the previous studies due to the large uncertainty of contamination in photometric LAE samples and the limited spectroscopic LAE samples.

Another open question in relation to the $\text{Ly}\alpha$ LF is the shape of the bright end. Several studies have attempted to statistically characterize the bright LAEs with $\log L_{\text{Ly}\alpha}/[\text{erg s}^{-1}] \gtrsim 43.5$ based on photometrically selected samples, reaching various conclusions. For example, Konno et al. (2016) identified an excess in the number density with respect to the Schechter function at the bright end of their $\text{Ly}\alpha$ LFs at $z = 2.2$. Such an excess was also found in $\text{Ly}\alpha$ LFs over other redshift ranges (e.g., Wold et al. 2017; Zheng et al. 2017). Sobral et al. (2017, 2018a), and Matthee et al. (2017) have shown a similar but less significant bright-end excess at $z = 2 - 3$ and demonstrated that such an excess can be fitted by a power law. At similar redshifts, Spinoso et al. (2020) found $\sim 14,500$ LAEs with $\log L_{\text{Ly}\alpha}/[\text{erg s}^{-1}] > 43.3$. The $\text{Ly}\alpha$ LFs of their bright LAEs are described by Schechter exponential decays with $\log L_{\text{Sch}}^*/[\text{erg s}^{-1}] \sim 44.5 - 44.8$. Despite these efforts, the precise shape of the $\text{Ly}\alpha$ LF, especially at the bright end, is in need of further constraints from spectroscopic studies.

Along with the shape of the $\text{Ly}\alpha$ LF at the bright end, it is also important to understand the nature of the extreme objects that cause the bright-end excess. Although the differential attenuation of $\text{Ly}\alpha$ photons in the clumpy ISM may cause the $\text{Ly}\alpha$ LFs to have a non-

Shechter shape, more evidence attributes the bright-end excess to the existence of Ly α -emitting active galactic nuclei (AGN). The AGN activity peaks at $z \sim 2 - 3$ (Hasinger 2008), which may result in the contribution of faint AGN to the LAE population. Such a scenario is supported by results based on the spectroscopic follow-ups and multi-wavelength detections of small samples of photometrically-selected, bright LAEs. In particular, Ouchi et al. (2008) show that their bright LAEs at $z = 3.1 - 3.7$ with $L_{\text{Ly}\alpha} = 10^{43.3-43.6} \text{ erg s}^{-1}$ always host AGN. Sobral et al. (2018b) conduct spectroscopic observations on 21 luminous LAEs at $z \sim 2 - 3$ and conclude that the AGN fraction increases with Ly α luminosity. Similar trends are also observed through the number fraction of radio and X-ray detected LAEs (e.g., Matthee et al. 2017; Calhau et al. 2020). AGN trace the growth of black holes (BHs) at the center of galaxies and may provide feedback that suppresses star formation in galaxies (e.g., Fabian 2012; Merloni & Heinz 2013). Hence, they are keys to understanding galaxy evolution.

In this paper, we investigate the Ly α and UV LFs of LAEs at $z \sim 2 - 3$ detected by the Hobby-Eberly Telescope Dark Energy Experiment (HETDEX) survey (Hill et al. 2008; Gebhardt et al. in preparation; Hill et al. in preparation). Combining the un-targeted, wide-field integral field spectroscopic (IFS) data of HETDEX and deep ground-based imaging data of Subaru Hyper Supreme Cam (HSC), we explore the low number density regime for both Ly α and UV LFs, where the LAE population consists of both SF galaxies and AGN.

This paper is arranged as follows. Section 2 describes the details of the HETDEX survey and the spectroscopic data included in this paper. Our LAE samples are presented in Section 3. In Section 4, we derive the Ly α LF at $z = 2.0 - 3.5$. We also show the spectroscopic properties and the UV LF of type 1 AGN in our LAE samples. We discuss the evolution of the Ly α LF of LAEs and the UV LF of type 1 AGN in Section 5. Throughout this paper, we use AB magnitudes (Oke 1974) and the cosmological parameters of $(\Omega_m, \Omega_\Lambda, h) = (0.3, 0.7, 0.7)$.

2. OBSERVATIONS AND DATA

2.1. HETDEX Survey

HETDEX is an un-targeted integral field spectroscopic survey designed to measure the expansion history of the universe at $z \sim 1.9 - 3.5$ by mapping the three-dimensional positions of around 1 million LAEs. The survey started in January 2017, and is scheduled to complete in 2024. On completion, it will cover $\sim 540 \text{ deg}^2$ of sky area that is divided into northern ("Spring") and equatorial ("Fall") fields. The corresponding survey

volume is ~ 11 comoving Gpc 3 . The survey is conducted with the Visible Integral-field Replicable Unit Spectrograph (Hill et al. 2018a; Hill et al. in preparation), which is fed by fibers from the prime focus of the upgraded 10m Hobby-Eberly Telescope (HET, Ramsey et al. 1994; Hill et al. 2018b; Hill et al. in preparation). VIRUS is a replicated integral field spectrograph (Hill 2014) that consists of 156 identical spectrographs (arrayed as 78 units, each with a pair of spectrographs) fed by 34,944 fibers, each 1."5 diameter, projected on sky. VIRUS has a fixed spectral bandpass of 3500 – 5500 Å and resolving power $R \sim 800$ at 4500 Å (Hill et al. 2018a; Hill et al. in preparation). The fibers are grouped into 78 integral field units (IFUs, Kelz et al. 2014), each with 448 fibers in a common cable. There is one IFU covering $51'' \times 51''$ area for each two-channel spectrograph unit. The fibers are illuminated directly at the f/3.65 prime focus of HET and are arrayed within each IFU with a 1/3 fill-factor such that an observation requires three exposures with dithers in sky position to fill in the areas of the IFUs. For HETDEX, the exposure time is 3x360 seconds for each pointing set. The IFUs are arrayed in a grid pattern with 100 arcsecond spacing, within the central 18 arcmin diameter of the field of the upgraded HET, and fill this area with $\sim 1/4.5$ fill factor. A detailed technical description of the HET wide field upgrade and VIRUS and their performance is presented in Hill et al. (in preparation).

The data presented in this paper were obtained as part of the internal HETDEX data release 2 (iHDR2, Gebhardt et al., in preparation). iHDR2 includes 3086 exposure sets taken between January 2017 and June 2020 with between 16 and 71 active IFUs. From these data we select 1862 exposure sets whose footprints are covered by Subaru/Hyper Supreme-Cam (HSC) imaging data. The total area is 57 deg^2 with spatial filling factors of $\sim 20\%$, which yields an effective area of 11.4 deg^2 , corresponding to $\sim 2.0 \times 10^8$ comoving Mpc 3 for the redshift range of $2.0 < z < 3.5$.

2.2. Subaru HSC Imaging

To provide better measurements on the UV continua of LAEs at $z = 1.9 - 3.5$, we utilize the r -band imaging data taken by Subaru/HSC. The HSC r -band filter covers the wavelength range of 5500 \sim 7000 Å. For sources at $z = 1.9 - 3.5$, the HSC r -band magnitudes serve as a good estimation for the UV continua while the HETDEX spectra can detect the Ly α emission lines.

The r -band imaging data in this study are taken from two surveys, the HSC r -band imaging survey for HETDEX (hereafter HETDEX-HSC survey) and Subaru Strategic Program (HSC-SSP; Aihara et al. 2018).

HETDEX-HSC survey has obtained imaging data of a ~ 250 deg² area in the Spring field. The observations of the HETDEX-HSC survey were carried out in 2015-2018 (S15A, S17A, S18A; PI: A. Schulze) and 2019-2020 (S19B; PI: S. Mukae) with the total observing time of 3 nights and the seeing sizes of $0''.6 - 1''.0$. The 5σ limiting magnitude in a $3''.0$ diameter aperture is $r = 25.1$ mag.

In addition to the HETDEX-HSC survey, we also exploit the r -band imaging data in the public data release 2 (PDR2) of HSC-SSP (Aihara et al. 2019). The HSC-SSP PDR2 includes deep multi-color imaging data of a sky area of ~ 300 deg² taken over the span of 300 nights. The r -band imaging data of HSC-SSP PDR2 have average seeing size of $\sim 0''.7$. The 5σ limiting magnitude for the $3''.0$ diameter aperture is $r = 25.8$ mag and $r = 27.7$ mag in the Wide (W) and Ultra-Deep (UD) layers, respectively. The data reduction and source detection of HETDEX-HSC and HSC-SSP surveys are conducted with `hscPipe` (Bosch et al. 2018) version 6.7.

3. SAMPLES

In this section, we provide details of how we construct LAE samples with iHDR2. Although iHDR2 includes a curated emission line catalog (hereafter HETDEX emission line catalog) that is based on the blind search for detections from all spectral and spatial elements (Gebhardt et al., in preparation), the HETDEX emission line catalog fails to recover some of the previously identified type 1 AGN with broad emission lines. This is because the HETDEX emission line catalog is optimized for typical star-forming galaxies with narrow emission lines. Given the large HETDEX dataset, current attempts to include broad emission line candidates remain challenging, as this could introduce artifacts such as continuum between two close absorption lines and humps caused by calibration issues. With the challenge of selecting broad-line LAEs from the HETDEX emission line catalog, we construct a new emission line catalog based on the iHDR2 reduced fiber spectra and the deep HSC r -band imaging data (hereafter HSC-detected catalog). Our detection algorithm performs emission line detection in a variety of wavelength bins at the positions of continuum sources in the HSC r -band imaging data. Because the spatial positions are determined, the algorithm is able to detect broad emission line candidates while limiting the number of artifacts. In Section 3.1, we describe the HETDEX emission line catalog and the HSC-detected catalog. We combine the HETDEX emission line catalog and the HSC-detected catalog, making an emission line catalog with signal-to-noise ratio (S/N)

> 5.5 that does not miss broad emission lines. In Section 3.2, we construct the LAE sample from the combined catalog. Section 3.3 describes our spectroscopic follow-ups on LAE candidates selected in Section 3.2.

3.1. Emission Line Catalogs

3.1.1. HETDEX Emission Line Catalog

The HETDEX emission line catalog (internally v2.1.1) is constructed with an automatic detection pipeline developed by the HETDEX collaboration. Details of the pipeline are introduced in Gebhardt et al. (in preparation). In general, the following three steps are involved. i) The positions of emission line candidates are determined based on a grid search in all spatial and spectral elements of the reduced HETDEX fiber spectra with bin sizes of $0''.5$ in the spatial direction and 4\AA in the wavelength direction. ii) At the positions of detections, 1D spectra are extracted, and emission line fits are conducted to measure the central wavelengths, fluxes, and linewidths of emission line candidates. iii) Emission line candidates are further screened based on the χ^2 of the fitting results, S/N, and linewidths.

From the HETDEX emission line catalog, we obtain emission line candidates with $S/N > 5.5$ and wavelength of $3666 \text{\AA} < \lambda < 5490 \text{\AA}$. The $S/N > 5.5$ cut allow us to obtain a relatively clean emission line sample with limited false detections. We apply the wavelength cut to keep consistency with our HSC-detected sources (Section 3.1.2). We also require the emission line candidates to locate within the areas covered by HSC r -band imaging data. We measure the rest-frame UV continua of emission line candidates using the HSC r -band imaging data. We cross-match the emission line candidates with the HSC r -band detected sources within $2''$ radii, and use the $3''$ diameter aperture magnitudes of the r -band detected sources as the continua flux density. If there are no r -band detected counterparts, we use the 5σ limiting magnitude (Table 2) as the upper limit of the continua flux density.

To check the possible contamination from false detections such as cosmic rays, sky residuals, and bad pixels, we randomly select 412 emission line candidates and conduct visual classification. We find that 17/412 (4%) emission line candidates are false detections. This indicates a negligible fraction of false detections in our HETDEX emission line catalog. We obtain 138314 emission line candidates from the HETDEX emission line catalog.

3.1.2. HSC-Detected Catalog

We construct our HSC-detected emission line catalog based on the r -band imaging data of the HETDEX-HSC survey and the HSC-SSP survey. From the r -band de-

tected source catalog, we select isolated or cleanly deblended sources. We then require that none of the central 3×3 pixels are saturated, and none of the central 3×3 pixels are severely affected by very bright neighboring sources. We also remove objects with flags indicating failed centroid position measurements. The selection criteria that we use for this purpose are listed in Table 1. We then limit the catalog to the 2972750 sources whose S/N is larger than 5 based on their $3''$ diameter aperture magnitudes.

We extract 1D source spectra $F_{\text{source}}(\lambda)$ at the positions of the objects in the r -band source catalog from the reduced HETDEX fiber spectra. We assume that the 2D distribution of light on the focal plane for point-sources is described by the Moffat PSF (e.g. Moffat 1969; Trujillo et al. 2001), and calculate the PSF value p_i at the position of fiber i . We sum up the fiber spectra within a radius of $2.''5$ around the positions of the objects in the r -band source catalog using the equation:

$$F_{\text{source}}(\lambda) = \frac{\sum_{i=1}^n F_i(\lambda)p_i}{\sum_{i=1}^n p_i^2}, \quad (2)$$

where $F_i(\lambda)$ is the spectrum of fiber i . Since the noise levels of fiber spectra at the edge of the HETDEX spectral range is > 3 times higher than the median level, we only use the data in the spectral range of $3666 \text{ \AA} < \lambda < 5490 \text{ \AA}$. This wavelength range corresponds to the Ly α redshift of $2.0 < z < 3.5$.

We perform emission line detection and flux measurement on the source spectra. We first subtract continua from the source spectra with the median filter and sigma clipping method. To include the broad emission lines, we then repeatedly scan and measure the S/N of the source spectra within various wavelength bins (6, 10, 18, 34, and 110 \AA). We require the emission lines to have $S/N > 5.5$ in any of the wavelength bins. We fit single Gaussian profiles to measure the central wavelengths and FWHMs of the emission lines. Since the shapes of Ly α emission lines are sometimes asymmetric or have double peaks (e.g. Dijkstra et al. 2006; Matthee et al. 2018), we additionally fit double Gaussian profiles. For flux measurements, the choice between the single Gaussian and the double Gaussian models are determined by visual inspections.

To remove false detections such as cosmic rays, sky residuals, and bad pixels, we first apply the machine learning (ML) classifier (Sakai 2021, Sakai et al., in preparation) that takes the 2D spectrum of each emission line candidate as input and returns a score from 0 (false detections) to 1 (real detections). We test the reliability of our ML classifier by visually classifying 14276 randomly selected detections. Among the 14276 detec-

tions, 1725(12551) are classified as real(false) detections. Comparing our visual classification with the scores given by the ML classifier, we find that a score higher than 0.1 effectively remove 5762/12551(46%) false detections while recovering 1624/1725(94%) real detections. We thus require a score higher than 0.1. This initial screening process yields to 385493 emission line candidates from the HSC-detected catalog. We conduct visual classification to remove the remaining false detections in the HSC-detected catalog after selecting LAE candidates in Section 3.2.

3.2. LAE Selection

It is challenging to distinguish Ly α from [OII] $\lambda 3727 \text{ \AA}$ lines with the HETDEX spectral data alone for three reasons. First, the spectral resolution of VIRUS is not high enough to distinguish between the asymmetric Ly α and the blended [OII] doublet based on the skewness of their emission line profiles (Hill et al. in preparation; Gebhardt et al. in preparation). Second, many LAEs at $2.06 \leq z \leq 3.5$ and [OII] emitters at $0.1 \leq z \leq 0.5$ appear as single-line emitters in the HETDEX spectra whose range is $3500 - 5500 \text{ \AA}$. Finally, the relatively low sensitivity makes it difficult to precisely measure the continuum of sources within the spectrum alone to select LAEs with the rest-frame equivalent width (EW_0) cut technique (e.g. Gronwall et al. 2007; Ouchi et al. 2008; Konno et al. 2016) that is widely used.

To resolve this problem, we identify Ly α emission lines from the final emission line catalog based on the EW_0 calculated from the flux measured from HETDEX spectra and continuum measured from HSC r -band imaging data. Our goal is to select Ly α emission lines from both SF galaxies and AGN. We first require the EW_0 of the emission line to be greater than 20 \AA , assuming Ly α redshifts. This Ly α EW_0 cut is similar to previous LAE studies (e.g. Gronwall et al. 2007; Konno et al. 2016). We estimate continuum flux densities at the wavelength of Ly α from the HSC r -band magnitudes with the assumption of a flat UV continuum (i.e., $F_\nu = \text{const}$). This is a typical UV spectrum assumed in studies on high- z galaxies including LAEs (e.g., Ouchi et al. 2008; Konno et al. 2016, 2018). At $z = 2 - 3.5$, the r -band central wavelength corresponds to the rest-frame $1400 - 2000 \text{ \AA}$. If we assume a UV slope of -0.5 to 0.5 , the resulting UV flux changes by only 20%.

We notice that with this Ly α EW_0 cut, there still remain a consistent number of foreground contaminants. Most of these contaminants are the [OII] (CIV $\lambda 1549 \text{ \AA}$, CIII] $\lambda 1909 \text{ \AA}$, and MgII $\lambda 2798 \text{ \AA}$) emission lines from low- z SF galaxies (AGN). Because the sources of contamination are different for SF galaxies and AGN, it is

Table 1. Flags for the HSC r -band source catalog

Parameter	Value	Notes
r_pixelflags_edge	False	Source is outside usable exposure region
r_pixelflags_interpolatedcenter	False	Interpolated pixel in the source center
r_pixelflags_saturatedcenter	False	Saturated pixel in the source center
r_pixelflags_crcenter	False	Cosmic ray in the source center
r_pixelflags_bad	False	Bad pixel in the source footprint
r_pixelflags_bright_objectcenter	False	Source center is close to BRIGHT_OBJECT pixels
r_pixelflags_bright_object	False	Source footprint includes BRIGHT_OBJECT pixels
r_pixelflags	False	General failure flag
detect_istractinner	True	True if source is in the inner region of a coadd tract
detect_ispatchinner	True	True if source is in the inner region of a coadd patch

difficult to select Ly α emission lines from SF galaxies and AGN with one set of criteria. To resolve this problem, We use the FWHM of the emission line to separate SF galaxies and type 1 AGN (e.g., [Netzer 1990](#)). We divide our $EW_0 > 20 \text{ \AA}$ emission line sample into two subsamples, narrow line (NL, $FWHM \leq 1000 \text{ km s}^{-1}$) and broad line (BL, $FWHM > 1000 \text{ km s}^{-1}$) subsamples, that mainly contain SF galaxies and type 1 AGN, respectively. We select NL-(BL-) LAEs from NL (BL) subsample, combining them to make our combined LAE (C-LAE) sample. Section 3.2.1 and 3.2.2 discuss NL- and BL- LAE selection respectively. We summarize our LAE sample in Section 3.2.3.

3.2.1. NL-LAE Subsample

We select NL-LAEs from the NL emission line catalog with $EW_0 > 20 \text{ \AA}$ and $FWHM \leq 1000 \text{ km s}^{-1}$. For the typical SF galaxy, the most prominent emission lines within the HETDEX spectral range of $3500 - 5500 \text{ \AA}$ could be Ly α , [OII], H β $\lambda 4863 \text{ \AA}$, and [OIII] $\lambda 4960 \text{ \AA}$, $\lambda 5007 \text{ \AA}$. Assuming the single emission line to be H β at $z = 0 - 0.13$ ([OIII] at $z = 0 - 0.10$), the HETDEX spectra would cover other strong emission lines such as [OII] (H β) on the blue (red) side of the spectrum. Because other emission lines of LAEs at $z = 1.9 - 3.5$ ([OII] emitters at $z = 0.13 - 0.48$) lie beyond the HETDEX wavelength coverage, LAEs ([OII] emitters) would appear as single-line emitters in the HETDEX spectra. Due to this reason, LAEs at $z = 2.1 - 3.5$ and [OII] emitters at $z = 0 - 0.5$ are indistinguishable in the HETDEX spectra for typical SF galaxy. To isolate LAEs from [OII] emitters, we apply the Bayesian statistical method ([Leung et al. 2017](#)), as modified and implemented by [Farrow et al. \(2021\)](#) and [Davis et al. \(in preparation\)](#). The Bayesian statistical method calculates the probability $P_{\text{LAE}}(P_{[\text{OII}]})$ that a given source is an LAE ([OII] emitter) based on the EW_0 , the luminosity, and the wavelength of the source. The probability ratio $P_{\text{LAE}}/P_{[\text{OII}]}$ serves as the LAE selection cri-

terion. We test various possible LAE selection criteria ($P_{\text{LAE}}/P_{[\text{OII}]} > 1, 2, 5, 10, 20$) with the HETDEX iHDR2 data, where 37 (10) spectroscopically and photometrically identified LAEs (foreground contaminants) are included in our emission line catalog (e.g. [Kriek et al. 2015](#); [Laigle et al. 2016](#); [Tasca et al. 2017](#)) with $EW_0 > 20 \text{ \AA}$. For each possible LAE selection criterion, we make test samples of both confirmed LAEs and foreground contaminants that meet the criterion. We calculate fractions of confirmed LAEs (foreground contaminants) in the test samples to the total confirmed LAEs (test samples) that correspond to a sample completeness (contamination rate). We apply the criterion of $P_{\text{LAE}}/P_{[\text{OII}]} > 1$ that provides a reasonably high completeness of 76% ($=28/37$) and a reasonably low contamination rate of 13% ($=4/32$). The number of objects in our NL-LAE subsample is 16194. Figure 2 shows four examples of our NL-LAEs.

3.2.2. BL-LAE Subsample

We examine our BL-LAE selection criteria of $EW_0 > 20 \text{ \AA}$ and $FWHM > 1000 \text{ km s}^{-1}$. For type 1 AGN, the major strong permitted and semi-forbidden emission lines within the HETDEX spectral range are Ly α , CIV, CIII], and MgII. When a single broad emission line is presented in the HETDEX spectrum, it could be Ly α from AGN at $z = 2.0 - 3.5$, CIV from AGN at $z = 1.3 - 2.0$, CIII] from AGN at $z = 0.8 - 1.3$, or MgII from AGN at $z = 0.3 - 1.0$. However, our Ly α $EW_0 > 20$ cut would require AGN emitting CIV, CIII], and MgII to have a relatively large rest-frame EWs ($\gtrsim 25, 31$, and 46 \AA). Based on stacking analyses of 53 AGN spectra taken with Wide Field Camera 3 on the *HST*, [Lusso et al. \(2015\)](#) find that the typical rest-frame EWs of CIV and CIII] are about 5 times smaller than that of Ly α . The EWs of MgII are also $\gtrsim 3$ times smaller than those of Ly α for AGN ([Netzer 1990](#)). Thus, the effect of contamination from low- z type 1 AGN would be small. Discussions on the contamination of our BL-LAE sub-

Table 2. Summary of LAE samples

Field	(R.A., Decl.)	Area ^a	$N_{\text{NL-LAE}}$	$N_{\text{BL-LAE}}$	$N_{\text{C-LAE}}$	Imaging data	$r_{5\sigma}^b$
	(deg)	(arcmin ²)					(mag)
dex-Spring	(205.0, 51.3)	29470	11966	1532	13498	HET-HSC	25.1
dex-Fall	(21.5, 0.0)	11542	4129	584	4713	HSC-SSP(W)	25.8
COSMOS	(150.2, 2.3)	133	99	10	109	HSC-SSP(UD)	27.7
Total		41145	16194	2126	18320		

^aEffective survey area covered by HETDEX fibers.

^b 5σ limiting magnitude of imaging data for a 3'' diameter aperture.

sample is presented in Section 4.1. We confirm that $> 90\%$ of Ly α -emitting AGN at $2.0 < z < 3.5$ in the SDSS DR14 sample (Pâris et al. 2018) satisfy our selection criteria. We obtain the final sample of BL-LAEs that contains 2126 objects. We notice that 458/2126 BL-LAEs have secured redshift at $z = 2.0 - 3.5$ based on multiple emission lines identified in HETDEX spectra. Figure 3 shows four examples of our BL-LAEs.

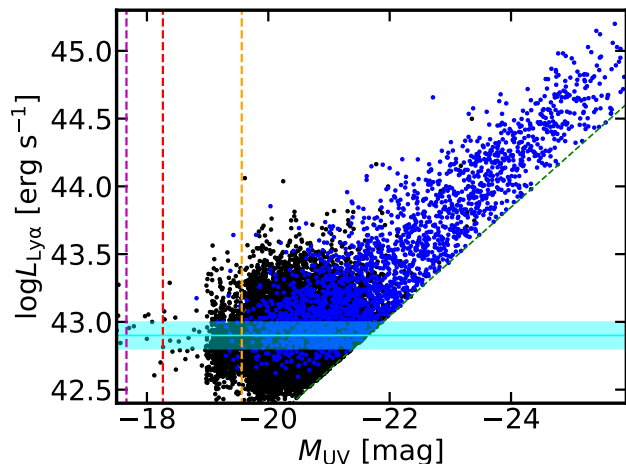


Figure 1. $M_{\text{UV}} - \log L_{\text{Ly}\alpha}$ distributions of our LAE sample. The blue (black) data points denote BL- (NL-) LAEs. The green dashed line indicates our $\text{EW}_0 > 20 \text{ \AA}$ cut. The horizontal cyan line corresponds to our 50% $L_{\text{Ly}\alpha}$ detection limit averaged over our redshift range, with cyan shaded regions indicating the 1σ uncertainty (68.27% equal-tailed credible interval). The magenta, red, and orange vertical dashed lines show the M_{UV} detection limits in COSMOS, Fall and Spring fields, respectively.

3.2.3. Summary of Our LAE Sample

Overall, our LAE selection criteria can be summarized as

$$\begin{aligned} & \text{EW}_0 > 20 \text{ \AA} \text{ and} \\ & [(\text{FWHM} \leq 1000 \text{ km s}^{-1} \text{ and } P_{\text{LAE}}/P_{[\text{OII}]} > 1) \\ & \text{or } (\text{FWHM} > 1000 \text{ km s}^{-1})] \quad (3) \end{aligned}$$

With this set of criteria, we select 18320 LAEs from an effective survey area of 11.4 deg². Our LAE sample includes 16194 (2126) NL- (BL-) LAEs (Table 2). In Figure 1, we show the $M_{\text{UV}} - \log L_{\text{Ly}\alpha}$ distribution of our LAE sample.

It should be noted that our LAEs defined by Equation 3 represent an EW_0 -limited sample of both Ly α -emitting SF galaxies and AGN at the bright $L_{\text{Ly}\alpha}$ regime ($L_{\text{Ly}\alpha} \gtrsim 10^{43} \text{ erg s}^{-1}$) that is different from the one of the forthcoming HETDEX studies, which produces a number count offset up to a factor of two.

3.3. Spectroscopic Follow-up of BL-LAE Candidates

To identify the potential CIV emission line of our type 1 AGN candidates, we carried out spectroscopic follow-up observations with the DEPT Imaging Multi Object Spectrograph (DEIMOS) on the Keck II Telescope (PI: Y. Harikane). With the criteria mentioned in Section 3.2.2, we select five BL-LAE candidates that are visible during the observations. Our targets are summarized in Table 3.

The observations were conducted on 2020 February 25 (UT) during the filler time of Harikane et al.'s observations when their main targets were not visible. The seeing size is $0''.4 - 0''.8$ in FWHM. We used 2 DEIMOS masks, KAKm1 and MUKm1, to cover the 5 objects (Table 3) with the BAL12 filter and the 600ZD grating that is a blue spectroscopy setting for DEIMOS. The slit width was $1''.0$. The spatial pixel scale was $0''.1181 \text{ pixel}^{-1}$. The spectral range is 4500-8000 \AA with a resolution of $R \sim 1500$. We took 5 (4) frames for

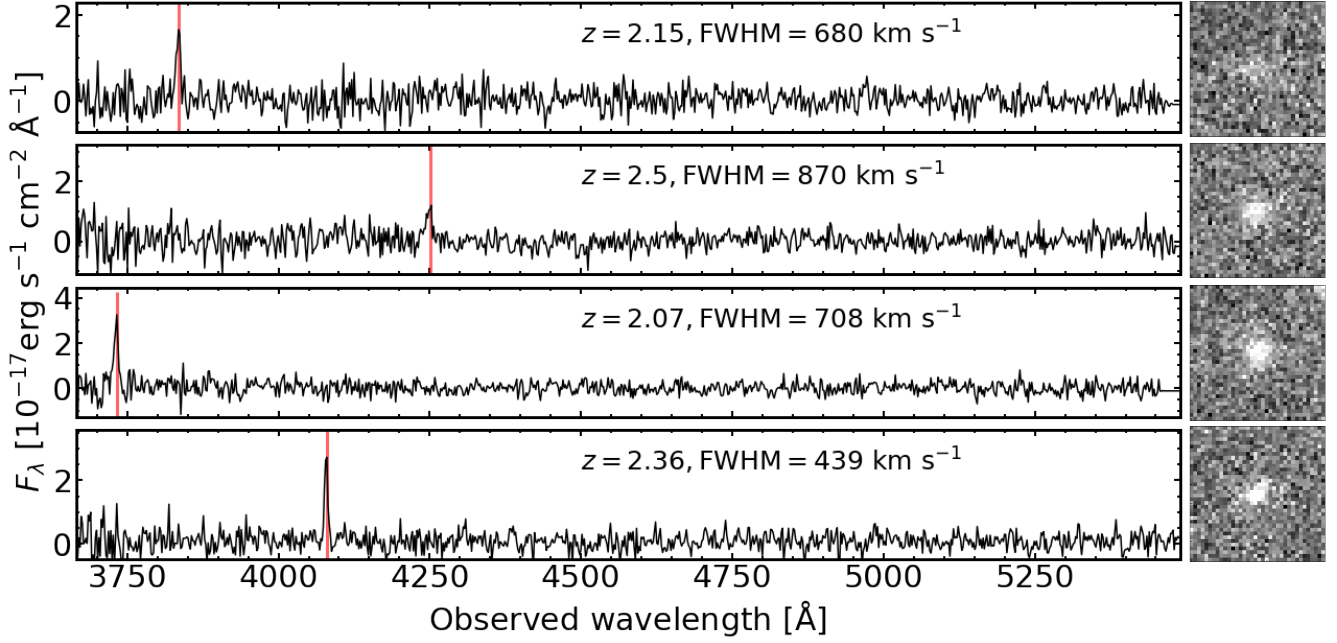


Figure 2. Examples of NL-LAEs. Left panels show the HETDEX spectra (black lines) of NL-LAEs. The redshifts and FWHMs are indicated at the top of each spectrum. The red solid lines represent the wavelengths of Ly α emission lines. Right panels denote the $8'' \times 8''$ r -band images from the HETDEX-HSC survey. North is up, and east is to the left.

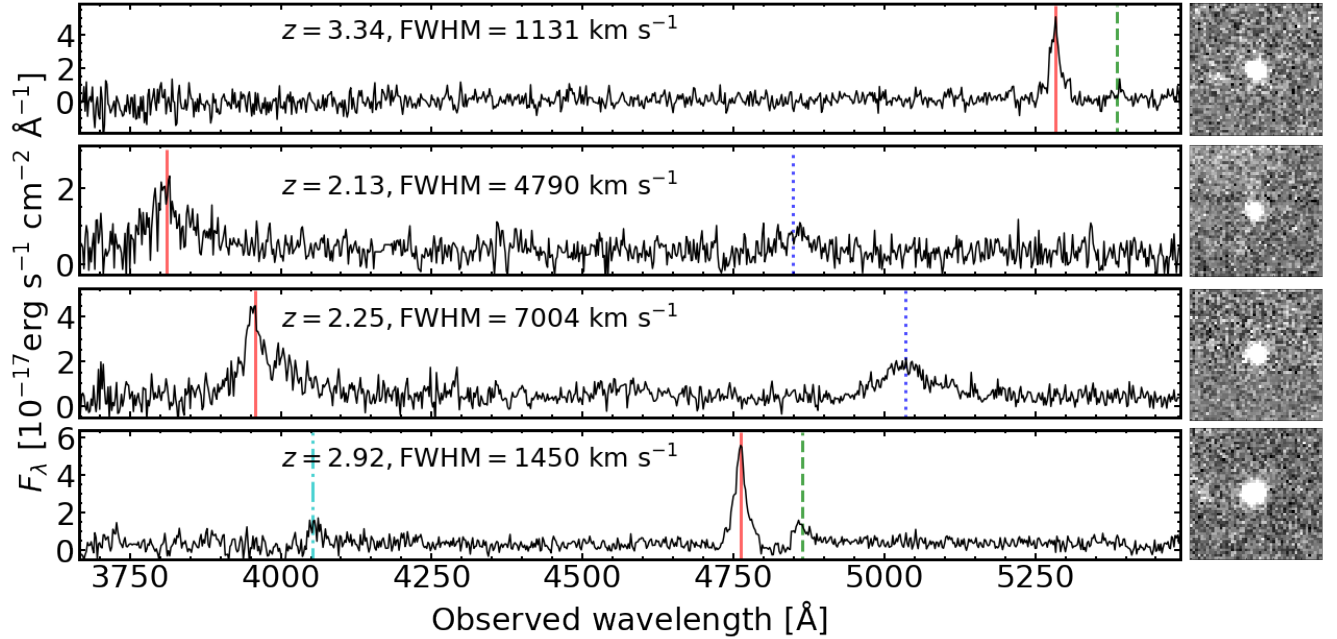


Figure 3. Same as Fig. 2, but for our BL-LAEs. Additionally, the blue dotted lines, green dashed lines, and cyan dash-dotted lines represent the wavelengths of detected C IV, N V $\lambda 1240$ Å, and O VI $\lambda 1035$ Å emission lines, respectively.

KAKm1 (MUKm1) with a single exposure time of 2,000 seconds. However, one frame for KAKm1 was affected by the high background sky level. We do not use this frame for our analysis. The total number of frames used

for our analyses is 4 for each mask, KAKm1 or MUKm1. The effective exposure time is 8,000 seconds. We acquired data of arc lamps and standard star G191B2B.

Table 3. Targets of our DEIMOS Observations

Object ID	R.A. (J2000)	Decl. (J2000)	$z_{\text{Ly}\alpha}$	$F_{\text{Ly}\alpha}$ (10^{-17} erg s $^{-1}$ cm $^{-2}$)	r (mag)	i (mag)	Note
ID-1	14:20:11.8258	+52:51:50.4864	2.33	23.04	26.4	26.5	No emission line detected
ID-2	14:19:23.4252	+52:51:50.4864	2.08	344.3	23.5	23.4	No data available
ID-3	14:18:46.2857	+52:41:48.9012	2.27	92.55	23.3	23.2	Foreground galaxy at $z = 0.48$
ID-4	14:19:28.9898	+52:49:59.3724	2.31	67.95	22.5	22.5	Type 1 AGN
ID-5	14:18:33.0739	+52:43:13.71	2.14	42.47	23.5	23.1	Type 1 AGN

We obtained spectroscopic data listed in Table 3. Because one out of 5 objects, ID-2, unfortunately fall on the broken CCD of DEIMOS, DEIMOS spectra are available for 4 out of 5 objects. Usually, the DEIMOS spectroscopic data are reduced with the `spec2d` IDL pipeline (Davis et al. 2003), which performs the bias subtraction, flat fielding, image stacking and wavelength calibration. However, the `spec2d` pipeline does not work in our blue spectroscopy setting due to the lack of wavelength data in the blue wavelength. We thus carry out the data reduction manually with the IRAF software package (Tody 1986), using the arc lamps for the wavelength calibration and standard star G91B2B for the flux calibration. We obtain 1D spectra of objects by summing up 15 pixels ($\sim 1''.77$) in the spatial direction.

We search for emission lines in both 2D and 1D spectra of the objects listed in 3 at the expected wavelengths, using the redshifts derived from the HETDEX Ly α emission lines. We identify CIV and CIII] emission lines in two out of the four faint BL-LAE candidates, ID-4 and ID-5. One of the four faint BL-LAE candidates, ID-3, is a foreground galaxy at $z = 0.48$ with H β and [OIII] emission lines identified in the DEIMOS spectrum. Another BL-LAE candidate, ID-1, has no detectable emission lines in the DEIMOS spectrum. The 3σ limiting flux of CIV (CIII]) of ID-1 is $2.16(1.87) \times 10^{-18}$ erg s $^{-1}$ cm $^{-2}$. Detailed spectroscopic properties of ID4 and ID5 are presented in Section 5.

4. DERIVING THE LUMINOSITY FUNCTIONS

4.1. Contamination

We estimate the contamination rate of our NL- (f_{NL}) and BL-LAEs (f_{BL}) by cross-matching our sample with spectroscopic and/or photometric catalogs. We also explore the morphology of BL-LAEs in archival *Hubble Space Telescope* (*HST*) imaging data. Because the number of objects available for f_{NL} (f_{BL}) estimation is not sufficient to build a redshift and luminosity correlation, we apply a uniform f_{NL} (f_{BL}) for our NL- (BL-) LAEs. The errors of f_{NL} and f_{BL} are based on Poisson statistics.

We estimate f_{NL} as described in Section 3.2.1. We make a subsample of 32 NL-LAEs in COSMOS field that are spectroscopically and/or photometrically identified by previous studies. We find that four out of these 32 known galaxies are foreground contaminants. We adopt the $f_{\text{NL}} = 13\% \pm 8\%$ (4/32) for our NL-LAE subsample.

For BL-LAEs, there are two types of contamination. The first type of contamination is the foreground type 1 AGN whose emission lines are redshifted to the HETDEX spectral range (Section 3.2.2). We estimate the fraction of such contamination $f_{\text{BL,foreground}}$ by cross-matching our BL-LAE subsample with SDSS DR14 QSO catalog (Pâris et al. 2018). Our crossmatching results shows that 111 of our BL-LAEs are previously identified AGN. Among these 111 objects, 99 objects are Ly α -emitting AGN at $z = 2 - 3.5$. The remaining 12 objects turn out to be foreground AGN (10 CIV-emitting AGN at $z \sim 1.4$, one CIII]-emitting AGN at $z \sim 1.0$, and one MgII-emitting AGN at $z \sim 0.8$). We thus apply $f_{\text{BL,foreground}} = 11\% \pm 3\%$ (12/111).

The second type of contamination is the broad emission line mimicked by blended narrow lines emitted from close-galaxy pairs on the sky at the similar wavelengths. We examine the morphology of BL-LAE candidates in COSMOS field with archival high-resolution optical images taken with Advanced Camera for Surveys (ACS) on *Hubble Space Telescope* (Koekemoer et al. 2007; Massey et al. 2010). We find that three out of 10 BL-LAE candidates have multiple components in the *HST*/ACS images that indicate possible close-galaxy pairs. Because the multiple components do not necessarily all have emission lines, we add errors allowing f_{close} to range from 0 to 30% + 20% (3/10). f_{BL} is obtained by:

$$f_{\text{BL}} = f_{\text{foreground}} + f_{\text{close}}. \quad (4)$$

4.2. Detection Completeness

For LAEs selected from HETDEX emission line catalog, the detection completeness (C_{HET}) as a function of observed wavelength (λ) and emission line flux (F) is estimated from simulated LAEs inserted into real HETDEX data (Farrow et al., in preparation; Gebhardt et al., in preparation). From λ and F , we cal-

culate Ly α redshift z and luminosity $L_{\text{Ly}\alpha}$, transforming $C_{\text{HET}}(\lambda, F)$ to $C_{\text{HET}}(z, L_{\text{Ly}\alpha})$. Figure 4 presents an example of $C_{\text{HET}}(z, L_{\text{Ly}\alpha})$.

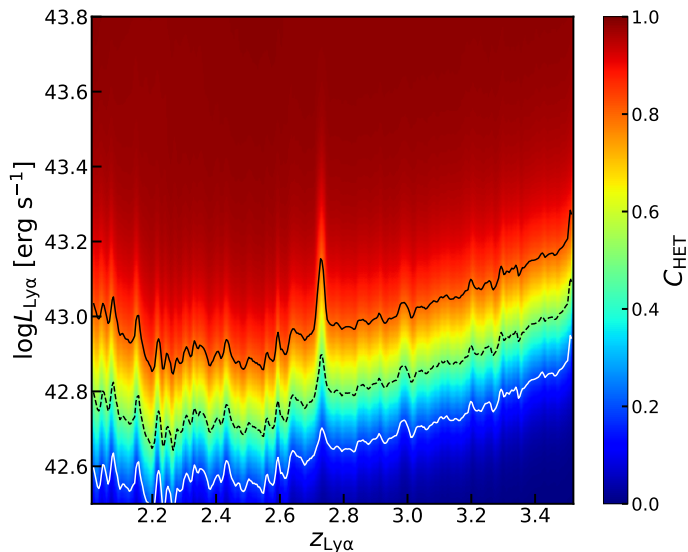


Figure 4. Completeness map of our HETDEX LAEs. The solid white line, dashed black line, and solid black line indicate the 20%, 50%, and 80% completeness levels, respectively.

For HSC-detected LAEs, the detection completeness C_{HSC} consists of two completeness values of the HSC r -band source detection $C_{\text{HSC,cont}}$ and the HETDEX emission line detection $C_{\text{HSC,line}}$, where

$$C_{\text{HSC}}(z, M_{\text{UV}}, L_{\text{Ly}\alpha}) = C_{\text{HSC,cont}}(z, M_{\text{UV}}) \times C_{\text{HSC,line}}(z, L_{\text{Ly}\alpha}). \quad (5)$$

We derive $C_{\text{HSC,cont}}$ from Kakuma (2020), who has calculated the completeness of their HSC-SSP r -band imaging data as a function of magnitude. We scale their completeness function by the difference of the 5σ limiting magnitudes between their HSC SSP wide field data ($r_{5\sigma} = 25.8$) and our HETDEX-HSC data ($r_{5\sigma} = 25.1$), estimating the completeness function of $C_{\text{HSC,cont}}$ that is shown in Figure 5.

We estimate $C_{\text{HSC,line}}$ by Monte Carlo simulations. Specifically, we make 500 mock spectra with Gaussian line models. For each object in our sample, we fix the FWHM of the line models to the emission line fitting result given in Section 3.1.2. We then produce composite fiber spectra, assuming the 2D light distribution is described by the Moffat PSF with a $2''$ FWHM value. We add noise to the composite fiber spectra, randomly generating the noise following a Gaussian distribution function whose sigma is the median value of the noise in the fiber spectra. We perform the emission-line detection on

the mock spectra in the same manner as Section 3.1.2, and calculate $C_{\text{HSC,line}}$ that is defined by the fraction of the detected artificial lines to the total mock spectra. We repeat this process with various z and $L_{\text{Ly}\alpha}$, obtaining $C_{\text{HSC,line}}(z, L_{\text{Ly}\alpha})$. An example of $C_{\text{HSC,line}}$ is shown in Figure 6.

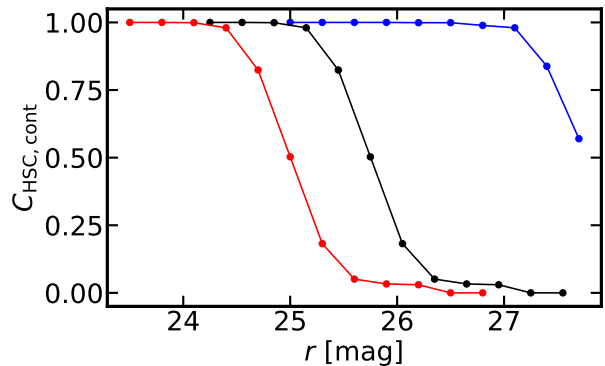


Figure 5. Completeness of our HSC r -band imaging data. The blue, black, and red line denote the completeness of imaging data in the COSMOS, Fall, and Spring field, respectively.

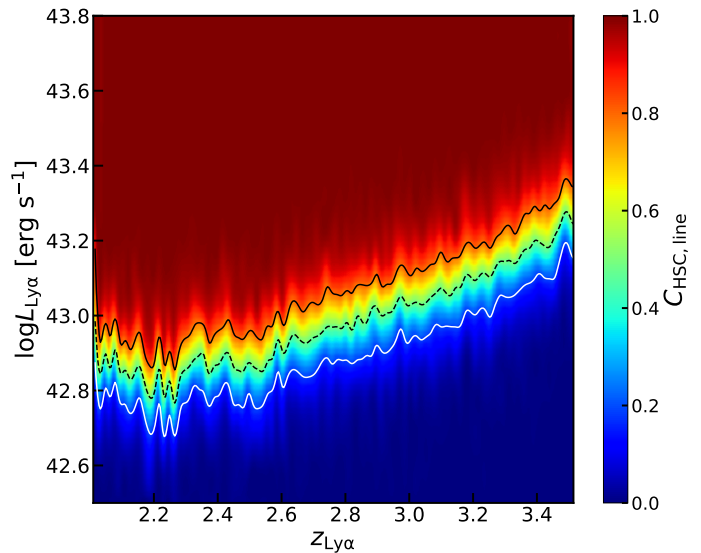


Figure 6. Same as Figure 4, but for our HSC-detected LAEs.

4.3. Ly α Luminosity Function

We derive the Ly α LF with our LAE sample. We apply the non-parametric $1/V_{\text{max}}$ estimator (Schmidt 1968; Felten 1976) that accounts for the redshift and lu-

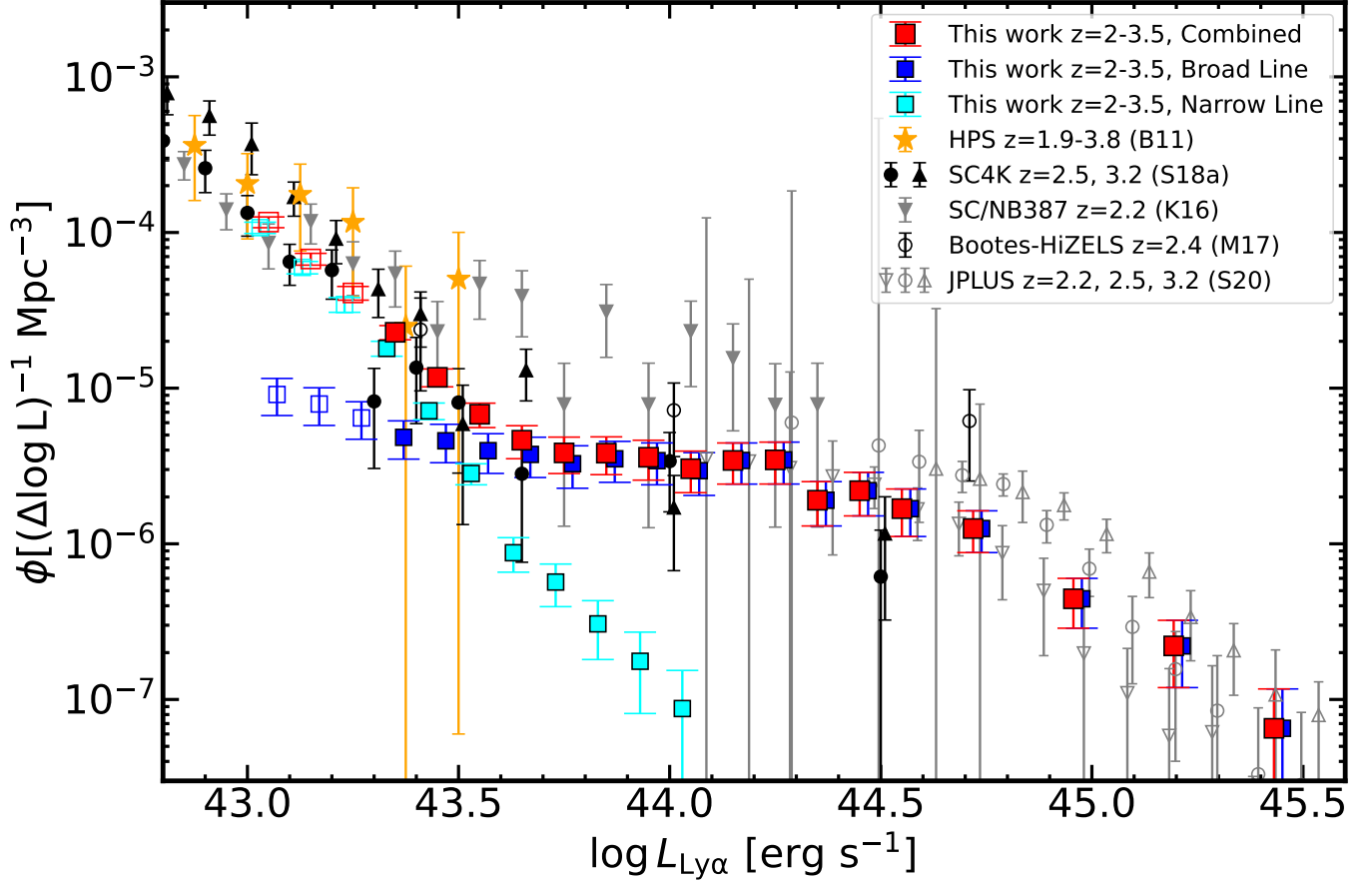


Figure 7. $\text{Ly}\alpha$ LF of our NL- (cyan squares), BL- (blue squares) and C-LAEs (red squares) within the 11.4 deg² survey area. Data points that may be affected by incompleteness due to Eddington bias is marked with open squares (see text). For clarity, we slightly shift the data points of NL- and BL-LAEs along the abscissa. The orange stars indicate the results from previous spectroscopic study of [Blanc et al. \(2011\)](#) at $1.9 < z < 3.8$ (B11). We also show the $\text{Ly}\alpha$ LFs at $\log L_{\text{Ly}\alpha}[\text{erg s}^{-1}] \gtrsim 43.3$ derived by previous photometric surveys/studies at three redshift slices of $z = 2.2$ (downwards triangles), $2.4\text{--}2.5$ (circles), and 3.2 (upwards triangles) that are taken from [Konno et al. \(2016\)](#) (K16, grey solid symbols), [Matthee et al. \(2017\)](#) (M17, black open symbols), [Sobral et al. \(2018a\)](#) (S18a, black solid symbols), and [Spinoso et al. \(2020\)](#) (S20, grey open symbols).

minosity dependent selection function of our LAE sample. For the i -th object in our LAE sample, $V_{\text{max},i}$ corresponds to the maximum comoving volume inside which it is detectable. The $V_{\text{max},i}$ value depends on the detection completeness functions $C_{\text{HET}}(z, L_{\text{Ly}\alpha})$ and $C_{\text{HSC}}(z, M_{\text{UV}}, L_{\text{Ly}\alpha})$,

$$V_{\text{max},i} = \omega \int_{z_{\text{min}}}^{z_{\text{max}}} C_i \frac{dV}{dz} dz, \quad (6)$$

where ω and $\frac{dV}{dz}$ denote the angular area of the survey and the differential comoving volume element, respectively. Here, z_{min} (z_{max}) is the lower (upper) limit of the redshift range of the survey. We calculate V_{max} of each NL- (BL-) LAE, $V_{\text{max}}^{\text{NL}}$ ($V_{\text{max}}^{\text{BL}}$), and obtain the number densities of NL- and BL-LAEs in each luminosity

bin with:

$$\phi_{\text{NL}}(\log L_{\text{Ly}\alpha}) = \frac{1 - f_{\text{NL}}}{\Delta(\log L_{\text{Ly}\alpha})} \sum_k \frac{1}{V_{\text{max},k}^{\text{NL}}}, \quad (7)$$

$$\phi_{\text{BL}}(\log L_{\text{Ly}\alpha}) = \frac{1 - f_{\text{BL}}}{\Delta(\log L_{\text{Ly}\alpha})} \sum_k \frac{1}{V_{\text{max},k}^{\text{BL}}}, \quad (8)$$

where $\Delta(\log L_{\text{Ly}\alpha})$ is the luminosity bin width and k is the number of objects in each luminosity bin. The summations in Eqs. (7) and (8) are performed over the k objects in each luminosity bin.

Figure 7 shows the binned $\text{Ly}\alpha$ LF of our LAE sample at $43.0 < \log L_{\text{Ly}\alpha}[\text{erg s}^{-1}] < 45.5$, where our LF reaches 50% completeness. Note that at $\log L_{\text{Ly}\alpha} < 43.3 \text{ erg s}^{-1}$, our $\text{Ly}\alpha$ LFs may suffer from a non-negligible Eddington bias ([Eddington](#)

1913) that is generated from uncertainties in HET-DEX spectro-photometry (Gebhardt et al., in preparation). We hence do not include the Ly α LF data points at $43.0 < \log L_{\text{Ly}\alpha}/[\text{erg s}^{-1}] < 43.3$ into our analysis. The error bars of our results are estimated from the quadrature sum of the Poissonian errors, errors in contamination correction, and flux measurement errors.¹ Our LFs span a wide Ly α luminosity range of $43.3 < \log L_{\text{Ly}\alpha}/[\text{erg s}^{-1}] < 45.5$, showing a significant bright-end excess at $\log L_{\text{Ly}\alpha}/[\text{erg s}^{-1}] \gtrsim 43.5$ that is dominated by BL-LAEs who are type 1 AGN with $\text{FWHM}(\text{Ly}\alpha) > 1000 \text{ km s}^{-1}$.

We compare our results in Figure 7 with those from previous studies at the similar redshift and $L_{\text{Ly}\alpha}$ ranges. At $z \sim 2 - 3$, Blanc et al. (2011) is the only work that presents the spectroscopically-derived Ly α LF at $\log L_{\text{Ly}\alpha}/[\text{erg s}^{-1}] \gtrsim 43$. Due to the limited survey area of 169 arcmin^2 and the small sample of 80 LAEs, their LF does not show a bright-end hump and has large errors in the two brightest $L_{\text{Ly}\alpha}$ bins at $\log L_{\text{Ly}\alpha}/[\text{erg s}^{-1}] \sim 43.3 - 43.6$. Over this $L_{\text{Ly}\alpha}$ range, our results are consistent with theirs while having significantly smaller errors. At $\log L_{\text{Ly}\alpha}/[\text{erg s}^{-1}] \sim 43.3 - 44$, our Ly α LFs are comparable with previous photometric studies (e.g., Konno et al. 2016; Matthee et al. 2017; Sobral et al. 2018a) given the relatively large scatter in their results, which can possibly be attributed to the different small redshift intervals probed by these NB surveys. At the brightest end with $\log L_{\text{Ly}\alpha}/[\text{erg s}^{-1}] \gtrsim 44$ where BL-LAEs dominate, our LF aligns well with Spinoso et al. (2020), supporting their suggestion that the bright LAEs in their sample are QSOs.

We conduct model fitting with our Ly α LF in Figure 7. In general, Ly α LFs at $\log L_{\text{Ly}\alpha} \lesssim 43.5 \text{ erg s}^{-1}$ are well described by the Schechter function. Because our Ly α LF does not cover $\log L_{\text{Ly}\alpha}/[\text{erg s}^{-1}] < 43.3$, we constrain the faint end of the Ly α LF by including the binned Ly α LF at $z = 2 - 3.2$ from Cassata et al. (2011) in our fitting. The Ly α LF of Cassata et al. (2011) is derived with spectroscopically identified LAEs whose $L_{\text{Ly}\alpha}$ range from $10^{41} - 10^{43} \text{ erg s}^{-1}$, hence complementary to our sample.

¹ We also evaluate the errors in luminosity distance measurements by considering the Ly α velocity offsets ($\Delta v_{\text{Ly}\alpha}$). Typical Ly α -emitting galaxies have $\Delta v_{\text{Ly}\alpha} \sim 200 - 300 \text{ km s}^{-1}$ (e.g., Verhamme et al. 2018). For AGNs at $z \sim 2 - 3$, we investigate $\Delta v_{\text{Ly}\alpha}$ based on SDSS DR14 QSO catalog (Rakshit et al. 2020). We find the 16th, 50th, and 84th percentiles of the $\Delta v_{\text{Ly}\alpha}$ distribution to be -301, 75, and 598 km s^{-1} , respectively. Assuming a $\Delta v_{\text{Ly}\alpha} = 598 \text{ km s}^{-1}$ would result in the uncertainty of $< 1\%$ in the luminosity, which is negligible compared with the bin widths of our LFs. We hence do not consider the errors in luminosity distances.

To parameterize the shape of the bright-end hump in our Ly α LF, we considering the following two models separately. In Model 1, we assume the bright-end follows a double power law (DPL) that is broadly used to describe the QSO/AGN UV LF (e.g., Boyle et al. 1988; Pei 1995; Boyle et al. 2000; Richards et al. 2006a; Stevans et al. 2018). The DPL is defined as

$$\phi_{\text{DPL}}(L_{\text{Ly}\alpha}) d\log L_{\text{Ly}\alpha} = \ln 10 \phi_{\text{DPL}}^* \left(\frac{L_{\text{Ly}\alpha}}{L_{\text{DPL}}^*} \right)^{-\alpha_{\text{DPL}}} + \left(\frac{L_{\text{Ly}\alpha}}{L_{\text{DPL}}^*} \right)^{-\beta_{\text{DPL}}} \Bigg]^{-1} d\log L_{\text{Ly}\alpha}, \quad (9)$$

where L_{DPL}^* , ϕ_{DPL}^* , α_{DPL} , and β_{DPL} are characteristic luminosity, the normalization factor, faint-end slope, and bright-end slope, respectively. In Model 2, we assume the bright-end can be described by a Schechter function as suggested by Spinoso et al. (2020).

We fit our binned Ly α LF with the function of

$$\phi(L_{\text{Ly}\alpha}) = \phi_{\text{Faint}}(L_{\text{Ly}\alpha}) + \phi_{\text{Bright}}(L_{\text{Ly}\alpha}), \quad (10)$$

where ϕ_{Faint} represents the Schechter function for the faint component, and ϕ_{Bright} is the DPL (Schechter) function of Model 1(2) for the bright component. We obtain posterior probability distributions for the free parameters in Equation 10 using the Markov Chain Monte Carlo (MCMC) technique. For the prior of L_{DPL}^* and L_{Sch}^* in ϕ_{Bright} , we assume uniform distributions that is larger than L_{Sch}^* in ϕ_{Faint} and smaller than the maximum observed $L_{\text{Ly}\alpha}$ ($10^{45.5} \text{ erg s}^{-1}$) in our Ly α LF. Since the number of our BL-LAEs at the luminosity brighter than the break of DPL in Model 1 is not large, we adopt a uniform prior for β_{DPL} in Model 1 covering a relatively narrow range of $[-5, -2]$ (e.g., Kulkarni et al. 2019). We assume broad, uniform priors for the other parameters. We use the emcee code (Foreman-Mackey et al. 2013) for MCMC. For each parameter, we adopt the posterior median as our best-fit value and the 68.27% equal-tailed credible interval as the uncertainty. The fitting results of our two models and the best-fit functions are presented in Table 4 and Figures 8, respectively. The posterior probability distributions of the parameters of Model 1(2) are shown in Figure 17 (18). We find that Model 1 can better describe the decay in our Ly α LF at $\log L_{\text{Ly}\alpha}/[\text{erg s}^{-1}] \gtrsim 44.8$ with smaller residuals, although the differences are smaller than 1σ . To compare the performance of the two models, We also calculate the difference in Bayesian information criterion (Schwarz 1978) that is defined as

$$\Delta \text{BIC} = \chi_2^2 - \chi_1^2 + (k_2 - k_1) \ln N. \quad (11)$$

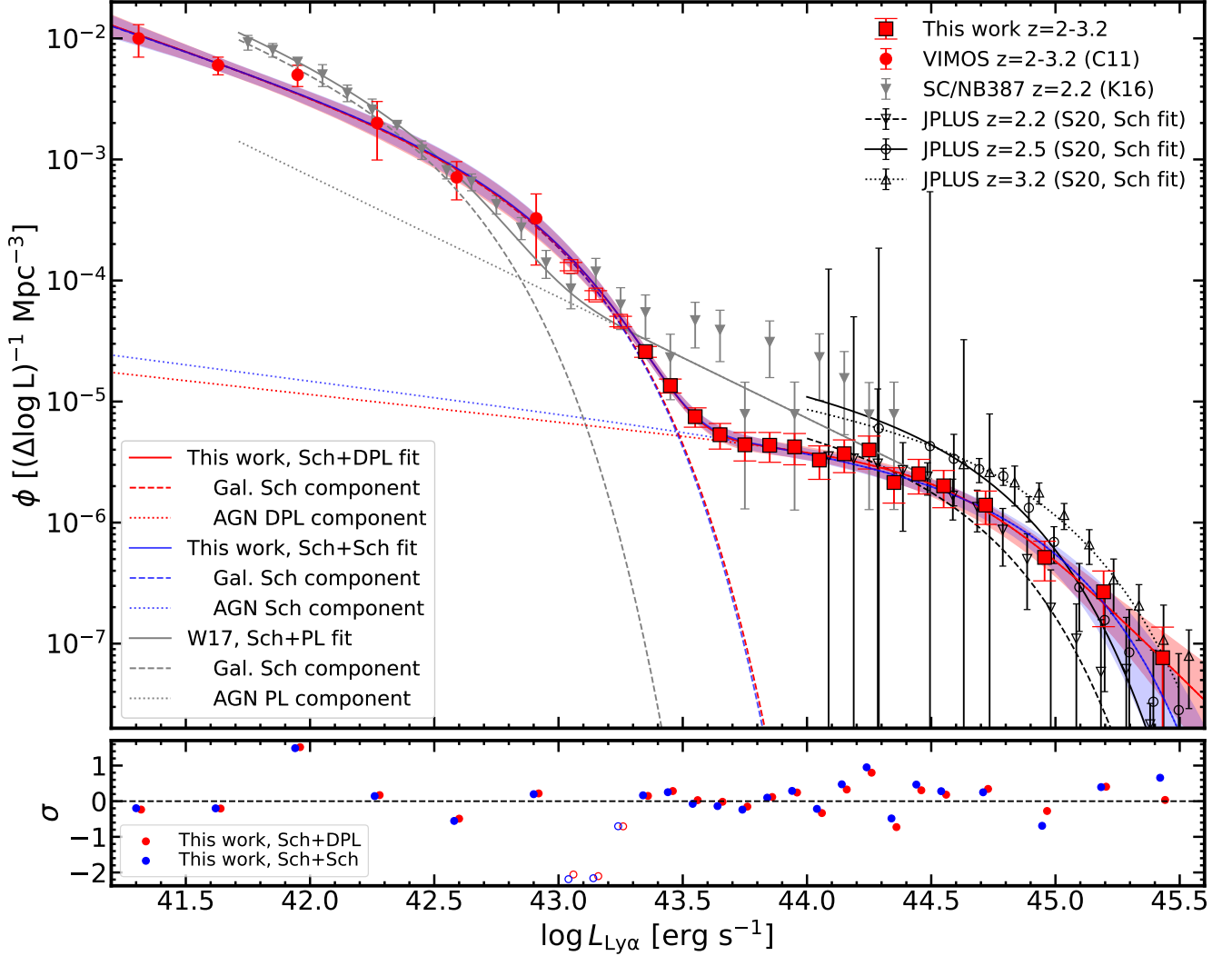


Figure 8. Top: Best-fit Ly α LF of our LAE sample with $2 < z < 3.2$ (red squares) and [Cassata et al. \(2011\)](#) at $2.0 < z < 3.2$ (red circles). The red (blue) line shows our best-fit result of Model 1(2) with the measurements of our study and [Cassata et al. \(2011\)](#), with shaded region corresponding to the 1σ uncertainty (68.27% equal-tailed credible interval). The black open downward triangles (black dashed line), circles (solid line), and upward triangles (dotted line) represents the binned Ly α LFs (best Schechter fit) from [Spinoso et al. \(2020\)](#) at $z \sim 2.25, 2.54,$ and $3.24,$ respectively. The grey triangles indicate the results from [Konno et al. \(2016\)](#). We also show in grey lines the fitting results from [Wold et al. \(2017\)](#) on the observed Ly α LF of [Konno et al. \(2016\)](#). The dashed, dotted, and solid grey lines indicate their best-fit Schechter component, power law component, and the overall LF, respectively. Bottom: The residuals of Model 1 (red) and 2 (blue) fit in units of the uncertainty in each luminosity bin.

Table 4. Fitting results of our Ly α LF

Model	Faint Component			Bright Component			
	α	$\log L^*$ [erg s $^{-1}$]	$\log \phi^*$ [Mpc $^{-3}$]	α	β	$\log L^*$ [erg s $^{-1}$]	$\log \phi^*$ [Mpc $^{-3}$]
Model 1 (Schechter+DPL)	$-1.70^{+0.13}_{-0.14}$	$42.87^{+0.09}_{-0.07}$	$-3.41^{+0.20}_{-0.24}$	$-1.23^{+0.42}_{-0.24}$	$-3.06^{+0.57}_{-0.90}$	$44.68^{+0.26}_{-0.40}$	$-5.92^{+0.26}_{-0.32}$
Model 2 (Schechter+Schechter)	$-1.69^{+0.13}_{-0.14}$	$42.86^{+0.09}_{-0.07}$	$-3.39^{+0.19}_{-0.23}$	$-1.27^{+0.23}_{-0.19}$	–	$44.85^{+0.19}_{-0.19}$	$-5.96^{+0.24}_{-0.27}$

In Equation 11, $\chi_1^2(\chi_2^2)$ and $k_1(k_2)$ is the χ^2 and the number of free parameters of Model 1(2), respectively,

and N represents the number of data points that are

used in the fitting. We find a ΔBIC value of -2.17 , suggesting that Model 1 is slightly favored over Model 2. We hence choose Model 1 (Schechter + DPL fit) as the best-fit model of our Ly α LF in the following discussions, although we cannot rule out a Schechter exponential decay of the Ly α LF at $\log L_{\text{Ly}\alpha} [\text{erg s}^{-1}] \gtrsim 45.8$ as described by Model 2.

We compare our best-fit model of Ly α LFs with previous studies. For the bright DPL component, our faint-end slope α_{DPL} is consistent with the results from Spinoso et al. (2020), who found an weighted-average α value of -1.35 ± 0.84 over their four redshift slices. For the faint component, our results have reasonably well constrained Schechter parameters L_{Sch}^* , α_{Sch} , and ϕ_{Sch}^* that are consistent with Cassata et al. (2011). We note that Cassata et al. (2011) fit their LF with a fixed L^* due to the lack of data at the bright end ($L_{\text{Ly}\alpha} > 10^{43} \text{ erg s}^{-1}$). Our results provide strong constraints at $L_{\text{Ly}\alpha} > L_{\text{Sch}}^*$, determining the best-fit Schechter function by fitting three Schechter parameters simultaneously.

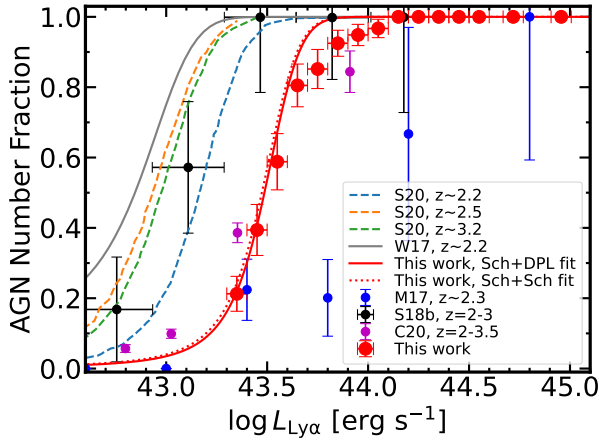


Figure 9. AGN number fraction as a function of $\log L_{\text{Ly}\alpha}$. Our results derived with Equation 12 are shown in the red circles. The functional form of our $f_{\text{AGN,Ly}\alpha}$ derived with Equation 13 using Model 1(2) is presented in the red solid (dashed) line. The other symbols represent previous measurements whose references are listed in the legend. M17: Matthee et al. (2017); W17: Wold et al. (2017); S18: Sobral et al. (2018b); C20: Calhau et al. (2020).

From our binned and best-fit Ly α LFs, we investigate the type 1 AGN number fraction ($f_{\text{AGN,Ly}\alpha}$) of our LAE sample. Note that our $f_{\text{AGN,Ly}\alpha}$ only accounts for type 1 AGN and hence represents the lower limit. First, we

calculate $f_{\text{AGN,Ly}\alpha}$ with

$$f_{\text{AGN,Ly}\alpha}(\log L_{\text{Ly}\alpha}) = \frac{\phi_{\text{BL}}(\log L_{\text{Ly}\alpha})}{\phi_{\text{BL}}(\log L_{\text{Ly}\alpha}) + \phi_{\text{NL}}(\log L_{\text{Ly}\alpha})}, \quad (12)$$

where ϕ_{NL} and ϕ_{BL} are the binned LFs defined in Equation 7 and 8, respectively. We present our results with those estimated with various types of AGN in Figure 9. Our $f_{\text{AGN,Ly}\alpha}$ increases rapidly with $L_{\text{Ly}\alpha}$, rising from $\sim 20\%$ to $\sim 90 - 100\%$ from $\log L_{\text{Ly}\alpha} / [\text{erg s}^{-1}] \sim 43.3$ to ~ 43.8 . Such a trend is in good agreement with the results derived with radio and X-ray detected AGN (Calhau et al. 2020). Matthee et al. (2017) also found a similar increase in $f_{\text{AGN,Ly}\alpha}(L_{\text{Ly}\alpha})$ using X-ray detected LAEs. At $\log L_{\text{Ly}\alpha} / [\text{erg s}^{-1}] \sim 43.6 - 44.4$, their results are lower than ours, which may be attributed to their relatively shallow X-ray and Ly α data (Calhau et al. 2020). Another study that discuss such an increase in $f_{\text{AGN,Ly}\alpha}(L_{\text{Ly}\alpha})$ is Sobral et al. (2018b) based on 21 spectroscopically identified objects that include both type 1 and type 2 AGN. At $\log L_{\text{Ly}\alpha} \leq 43.5 \text{ erg s}^{-1}$, our $f_{\text{AGN,Ly}\alpha}$ are lower than their results. The small sample and inclusion of type 2 AGN may explain the larger $f_{\text{AGN,Ly}\alpha}$ from Sobral et al. (2018b).

Second, we estimate $f_{\text{AGN,Ly}\alpha}$ with our best-fit Ly α LF, assuming that the faint Schechter component (bright DPL component) can well describe the Ly α LFs of SF galaxies (AGN). The similar method have been applied by Wold et al. (2017) and Spinoso et al. (2020) to derive $f_{\text{AGN,Ly}\alpha}(L_{\text{Ly}\alpha})$. However, as mentioned in Spinoso et al. (2020), $f_{\text{AGN,Ly}\alpha}(L_{\text{Ly}\alpha})$ estimated with this method only represents an illustrative results, given the strong assumption and the high sensitivity to the determination of the faint Schechter component. We calculate $f_{\text{AGN,Ly}\alpha}$ with

$$f_{\text{AGN,Ly}\alpha}(\log L_{\text{Ly}\alpha}) = \frac{\phi_{\text{Bright}}(\log L_{\text{Ly}\alpha})}{\phi_{\text{Bright}}(\log L_{\text{Ly}\alpha}) + \phi_{\text{Faint}}(\log L_{\text{Ly}\alpha})}. \quad (13)$$

As shown in Figure 9, our $f_{\text{AGN,Ly}\alpha}(L_{\text{Ly}\alpha})$ estimated with Equation 13 agrees nicely with the ones derived with Equation 12. Comparing with the results from Spinoso et al. (2020) that are based on their bright AGN/QSO LFs and the faint SF galaxy LFs from Sobral et al. (2018a), our $f_{\text{AGN,Ly}\alpha}(L_{\text{Ly}\alpha})$ has a similar increase, and shifts towards brighter $L_{\text{Ly}\alpha}$ by $\Delta \log L_{\text{Ly}\alpha} / [\text{erg s}^{-1}] \sim 0.3 - 0.5$. Wold et al. (2017) obtained a $f_{\text{AGN,Ly}\alpha}(L_{\text{Ly}\alpha})$ similar to Spinoso et al. (2020), but with a flatter increase, by fitting the observed LF from Konno et al. (2016) that has large scatters at the bright end. They also estimated the observed Ly α luminosity density contributed from SF galaxies ($\rho_{\text{Ly}\alpha,\text{SF}}^{\text{obs}}$) and AGN ($\rho_{\text{Ly}\alpha,\text{AGN}}^{\text{obs}}$) to be $10^{39.7}$

and $10^{39.5}$ erg s $^{-1}$ Mpc $^{-3}$, respectively, by integrating their best-fit Ly α LFs over the Ly α luminosity range of $\log L_{\text{Ly}\alpha} = 41.41 - 44.4$ erg s $^{-1}$. They concluded that at $z = 2.2$, AGN contribute to $\sim 40\%$ to the total observed Ly α luminosity density, which is consistent with their observational results at $z = 0.3$ and $z = 0.9$. We follow their method, calculating $\rho_{\text{Ly}\alpha, \text{SF}}^{\text{obs}}$ and $\rho_{\text{Ly}\alpha, \text{AGN}}^{\text{obs}}$ from our best-fit Ly α LF with

$$\rho_{\text{Ly}\alpha, \text{SF}}^{\text{obs}} = \int L_{\text{Ly}\alpha} \phi_{\text{Bright}}(L_{\text{Ly}\alpha}) dL_{\text{Ly}\alpha}, \quad (14)$$

$$\rho_{\text{Ly}\alpha, \text{AGN}}^{\text{obs}} = \int L_{\text{Ly}\alpha} \phi_{\text{Faint}}(L_{\text{Ly}\alpha}) dL_{\text{Ly}\alpha}. \quad (15)$$

We integrate Equations (14) and (15) over the same $L_{\text{Ly}\alpha}$ range as mentioned in Wold et al. (2017), obtaining the $\rho_{\text{Ly}\alpha, \text{SF}}^{\text{obs}}$ ($\rho_{\text{Ly}\alpha, \text{AGN}}^{\text{obs}}$) value of $10^{39.7}$ ($10^{38.6}$) erg s $^{-1}$ Mpc $^{-3}$. Despite the different shape of best-fit Schechter function as presented in Figure 8, our $\rho_{\text{Ly}\alpha, \text{SF}}^{\text{obs}}$ is consistent with the result from Wold et al. (2017). Contrastingly, our $\rho_{\text{Ly}\alpha, \text{AGN}}^{\text{obs}}$ is ~ 10 times lower, resulting in an AGN contribution of $\sim 8\%$ to the total Ly α luminosity density at $z = 2.0 - 3.2$.

4.4. UV LF

We derive the UV LF of our LAE sample in the same manner as described in Section 4.3. We convert the r -band magnitude (r) of our LAEs to the absolute UV magnitude (M_{UV}) using the following relation:

$$M_{\text{UV}} = r - 5 \log\left(\frac{d_L}{10 \text{pc}}\right) + 2.5 \log(1 + z) + K, \quad (16)$$

where d_L and z are the luminosity distance in pc and the redshift of our LAEs, respectively, determined by the Ly α emission lines in HETDEX spectra. We set the K -correction term (K) to be 0 according to our assumption of flat UV continua (Section 3.2). Figure 10 presents our UV LF at $-27 < M_{\text{UV}} < -21$, where the completeness reaches 50%. At the bright end with $M_{\text{UV}} < -22.5$, our results agree well with the SDSS QSO UV LF (Ross et al. 2013; Palanque-Delabrouille et al. 2016). Similar to our Ly α LF, the bright end of our UV LF are dominated by BL-LAEs, indicating the presence of type 1 AGN. At the faint end ($M_{\text{UV}} > -21.5$), our UV LF enters the SF galaxy regime where previous results on the UV LFs of LAEs and photometrically selected are available. Our results are generally consistent with previous UV LFs of LAEs derived by Ouchi et al. (2008) and Gronwall et al. (2007). Our LAE sample may suffer incompleteness at $M_{\text{UV}} > -21.3$ due to the detection limit of Ly α emission lines (Figure 1). As a result, only LAEs with strongest Ly α emission lines are included in

our sample. We denote our UV LF at $M_{\text{UV}} > -21.3$ with open symbols.

We study the LAE number fraction (X_{LAE}) as a function of M_{UV} based on our LAE UV LF ($\phi_{\text{UV, LAE}}$) and the best-fit UV LF of galaxies at $z \sim 3$ ($\phi_{\text{UV, } z=3}$) derived by Parsa et al. (2016). They obtained their galaxy sample based on multiband photometry with the photometric redshift determined by SED fitting. By assuming the galaxy sample of Parsa et al. (2016) is complete, we calculate X_{LAE} with:

$$X_{\text{LAE}}(M_{\text{UV}}) = \frac{\phi_{\text{UV, LAE}}(M_{\text{UV}})}{\phi_{\text{UV, } z=3}(M_{\text{UV}})}. \quad (17)$$

In Figure 11, we present our results covering $-22.1 < M_{\text{UV}} < -21.2$, where both our complete LAE UV LF and the galaxy UV LF are available. At $M_{\text{UV}} < -21$, our results show that X_{LAE} increases towards brighter UV luminosity. Such a trend is mainly due to BL-LAEs, whereas the number fraction of NL-LAEs does not change at $-22.5 \lesssim M_{\text{UV}} \lesssim -21$. We compare our results with the X_{LAE} values derived by two previous studies based on LBG samples at the similar redshift, Stark et al. (2010) and Kusakabe et al. (2020), both of which focused on SF galaxies without AGN. Stark et al. (2010) showed that X_{LAE} decreases with UV luminosity at $-22.5 < M_{\text{UV}} < -18.5$. Their X_{LAE} at $M_{\text{UV}} = -22$ is in agreement with our results derived from NL-LAEs alone. Contrastingly, Kusakabe et al. (2020) found no UV luminosity dependence of X_{LAE} at $M_{\text{UV}} \sim -20$ and -21 , though their values are consistent with those in Stark et al. (2010) within errors. Such a discrepancy may be caused by the increasing LBG selection bias towards faint M_{UV} (Kusakabe et al. 2020). Our results suggest that while the number fraction of SF-dominated LAEs has a tendency of decrease towards brighter UV luminosity, the number fraction of Ly α -emitting type 1 AGN becomes dominant at $M_{\text{UV}} \lesssim -21$ and increases towards brighter UV luminosity. This results in a turnaround of X_{LAE} at $M_{\text{UV}} \sim -21$. It should be noted that the UV LF of BL-LAEs shown here is calculated from the total UV flux that includes both AGN and stellar components of host galaxies. In Section 6.2, we evaluate the contributions of UV-continuum emission from AGN and their host galaxies based on SED fitting results from Kakuma (2020), and discuss the redshift evolution of AGN activities.

5. SPECTROSCOPIC PROPERTIES OF BL-LAEs

In this Section, we present spectroscopic properties of the two faint BL-LAEs with spectra, ID-4 and ID-5 (Table 3). We measure the central wavelengths, fluxes, and FWHMs of the C IV and C III] emission lines (Figure 12)

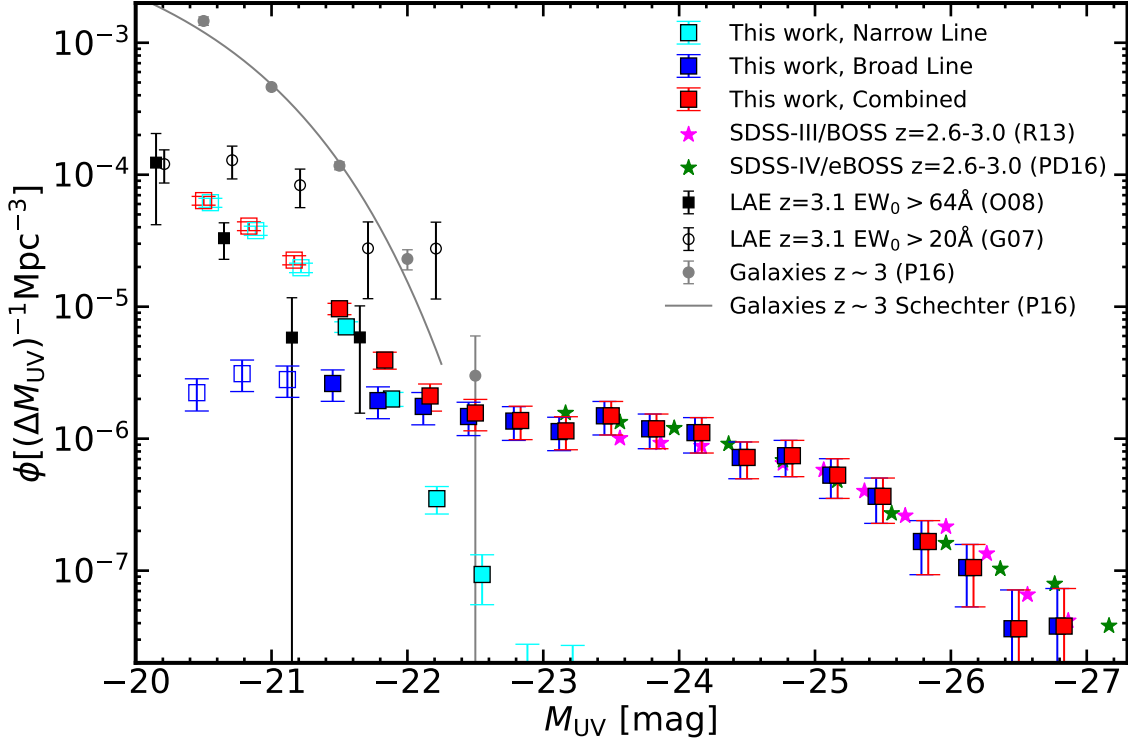


Figure 10. UV LF of our NL- (cyan squares), BL- (blue squares), and C-LAEs (red squares). Data points that may be affected by incompleteness is marked with open squares. The magenta and green stars denote the QSO UV LF at $z \sim 2.8$ from SDSS-III (Ross et al. 2013; R13) and SDSS-IV (Palanque-Delabrouille et al. 2016; PD16), respectively. The black squares and black open circles indicate the LAE UV LFs from Ouchi et al. (2008, O08) and Gronwall et al. (2007, G07), respectively. We also show the UV LF of photometrically selected galaxies at $z \sim 3$ in the grey circles and solid line (Parsa et al. 2016; P16).

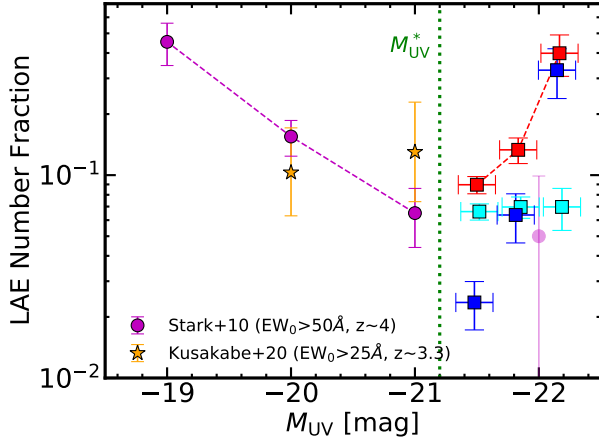


Figure 11. X_{LAE} as a function of M_{UV} . The red, blue, and cyan squares denote our results derived from C-, BL-, and NL-LAEs, respectively. The magenta circles and yellow stars represent the results from Stark et al. (2010) and Kusakabe et al. (2020), respectively. At M_{UV} fainter (brighter) than $M_{\text{UV}}^* \sim -21$, X_{LAE} increases (decreases) with M_{UV} .

in the spectra of ID-4 and ID-5 with a best-fit Gaussian

profile. We estimate the errors of fluxes and FWHMs by the Monte Carlo simulations. For each emission line, we make 1000 mock emission line spectra by adding noise to the observed line spectrum. The noise added to the observed line spectrum is generated, following a Gaussian probability distribution whose standard deviation is the 1σ uncertainty in the observed line spectrum. The errors of the measured fluxes and FWHMs are defined as the 68% confidence intervals in the distributions of the fluxes and FWHMs in the mock emission line spectra. We measure the FWHMs of C_{IV} and C_{III}], FWHM_{C_{IV}} and FWHM_{C_{III}}], to be $4043.2^{+138.8}_{-136.4}$ ($1072.2^{+96.8}_{-104.4}$) and $4268.0^{+373.7}_{-402.4}$ ($2024.1^{+485.6}_{-1202.6}$) km s⁻¹, respectively, for ID-4 (ID-5). For the C_{IV} emission line of ID-4, we find a broad component that cannot be well fitted with a single Gaussian profile. We fit the C_{IV} emission line of ID-4 with a double Gaussian profile that consists of a broad and a narrow components, measuring the FWHM with the broad component of the double Gaussian profile. We obtain FWHM_{C_{IV}} of the broad component is $5536.3^{+202.1}_{-185.8}$ km s⁻¹. Table 5 summarizes the emission line properties of our objects.

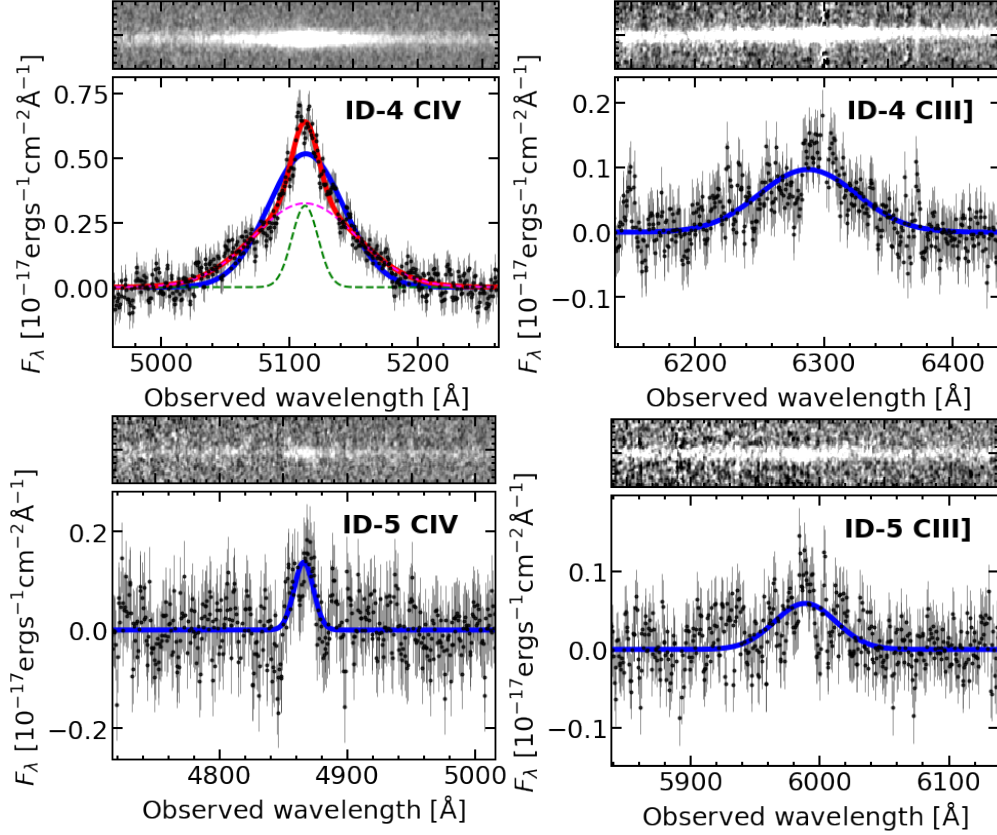


Figure 12. Emission line spectra of ID-4 and ID-5. At the top of each panel, we show the 2D spectrum. At the bottom of each panel, we present the 1D spectrum (black circles with errors) and the best-fit Gaussian profile (blue line). In the top-right panel, we also show the best-fit double Gaussian profile (red line) as well as the broad (cyan dotted line) and the narrow (green dotted line) component.

Table 5. Emission line properties

Object	Emission Line	Wavelength (Å)	Flux (10^{-17} erg s $^{-1}$ cm $^{-2}$)	FWHM (km s $^{-1}$)	Reduced χ^2
ID-4	CIV	5112.9	$37.83^{+1.06}_{-1.00}$	$4043.2^{+138.8}_{-136.4}$ ($5536.3^{+202.1}_{-185.8}$) ^a	1.157 (0.861) ^b
	CIII]	6287.7	$9.19^{+0.77}_{-0.75}$	$4268.0^{+373.7}_{-402.4}$	0.943
ID-5	CIV	4865.8	$2.50^{+0.35}_{-0.34}$	$1072.2^{+95.8}_{-104.4}$	1.043
	CIII]	5988.6	$2.50^{+0.57}_{-1.00}$	$2024.1^{+485.6}_{-1202.6}$	1.326

^a The number in the parenthesis indicate the FWHMs of the broad component in the two-component Gaussian fit.

^b The number in the parenthesis indicate the reduced χ^2 of the two-component Gaussian fit.

We use the scaling relations of Kim et al. (2018) with FWHM_{CIV} and the monochromatic continuum luminosity at rest-frame 1350\AA (L_{1350}) to derive the black hole masses M_{BH} of ID-4 and ID-5. We estimate L_{1350} by the log-linear extrapolation from the observed r -band and i -band fluxes as listed in Table 3. The M_{BH} value

is obtained with:

$$\log\left(\frac{M_{\text{BH}}}{M_{\odot}}\right) = A + \log\left\{\left(\frac{L_{1350}}{10^{44} \text{ erg s}^{-1}}\right)^{\beta} \left(\frac{\text{FWHM}_{\text{CIV}}}{1000 \text{ km s}^{-1}}\right)^{\gamma}\right\}. \quad (18)$$

We adopt the parameters (A, β, γ) of (6.7, 0.5, 2.0) that are taken from Kim et al. (2018). Our two faint BL-LAEs, ID-4 and ID-5, have the black hole masses of $\log(M_{\text{BH}}/M_{\odot}) = 8.70^{+0.03}_{-0.03}$ and $6.85^{+0.08}_{-0.08}$, respectively.

From the M_{BH} values, we calculate the Eddington ratio (λ_{Edd}) of a black hole that is defined as:

$$\lambda_{\text{Edd}} = L_{\text{bol}}/L_{\text{Edd}}, \quad (19)$$

where L_{bol} (L_{Edd}) is the bolometric (Eddington) luminosity of the black hole. The L_{bol} are derived from L_{1350} with the bolometric correction factor presented in Richards et al. (2006b) and Shen et al. (2011):

$$L_{\text{bol}} = 3.81 \times L_{1350}. \quad (20)$$

We derive the L_{bol} values of $10^{45.62}$ ($10^{44.82}$) erg s^{-1} for ID-4 (ID-5). The L_{Edd} is defined as:

$$L_{\text{Edd}} = 1.26 \times 10^{38} \left(\frac{M_{\text{BH}}}{M_{\odot}} \right). \quad (21)$$

The Eddington ratios of ID-4 and ID-5 are $\lambda_{\text{Edd}} = 0.067_{-0.004}^{+0.005}$ and $= 0.746_{-0.121}^{+0.111}$, respectively. Figure 13 presents the $M_{\text{BH}} - L_{\text{bol}}$ relation for ID-4 and ID-5.

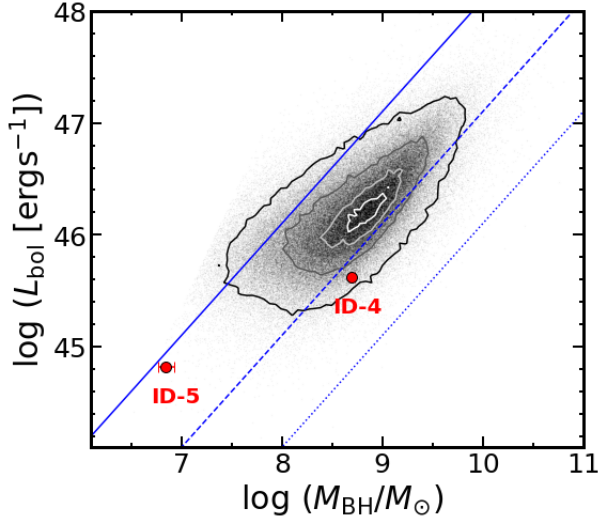


Figure 13. $M_{\text{BH}} - L_{\text{bol}}$ relation for ID-4 and ID-5. The red circles show our measurements. The grey data points and contours represent the results of $z = 2 - 3.5$ quasars in SDSS DR14 (Rakshit et al. 2020). The blue solid, dashed and dotted line correspond to the Eddington ratio $\lambda_{\text{Edd}} = 1, 0.1$ and 0.01 , respectively.

6. DISCUSSION

6.1. Faint end slope of $\text{Ly}\alpha$ LF

Although Gronke et al. (2015) have predicted the evolution of the faint end slope α_{Sch} of the $\text{Ly}\alpha$ LF based on a phenomenological model, such evolution has yet to be confirmed by observations. Combining our $\text{Ly}\alpha$ LF at $L_{\text{Ly}\alpha} \geq 10^{43.3} \text{ erg s}^{-1}$ and the one derived by Casata et al. (2011) at $L_{\text{Ly}\alpha} \leq 10^{43} \text{ erg s}^{-1}$, we reduce

the degeneracy in L_{Sch}^* and α_{Sch} and obtain α_{Sch} by fitting the three Schechter parameters simultaneously. To study the evolution of the faint end slope of the $\text{Ly}\alpha$ LF, we compare our result with α_{Sch} derived from previous photometric (Konno et al. 2018; Sobral et al. 2018a) and spectroscopic (Drake et al. 2017; Herenz et al. 2019) studies. We fit a linear relationship between α_{Sch} and z to the measurements from this work and Drake et al. (2017) in Figure 14. Our best-fit linear function has a slope of $-0.38_{-0.26}^{+0.18}$ and an intersection of $-0.71_{-0.60}^{+0.86}$. To evaluate the strength of the linear relation between α_{Sch} and z , we calculate the Pearson correlation coefficient r . We obtain the result of $r = -0.72$ with a p -value of 0.15, indicating a marginally significant trend of anti-correlation between α_{Sch} and z . Comparison between the $\alpha_{\text{Sch}} - z$ relation of the $\text{Ly}\alpha$ LF and that for the galaxy UV LF (Parsa et al. 2016) suggests that the α_{Sch} of the $\text{Ly}\alpha$ LFs is steeper than that of the galaxy UV LFs. Also, the evolution of α_{Sch} of the $\text{Ly}\alpha$ LF is more rapid than that of galaxy UV LF. The steepening of α_{Sch} of the $\text{Ly}\alpha$ LFs towards higher redshift is consistent with the observational results that dust attenuation of $\text{Ly}\alpha$ emission from SF galaxies decreases towards fainter UV luminosity (e.g., Ando et al. 2006; Ouchi et al. 2008) and higher redshift (e.g., Blanc et al. 2011; Hayes et al. 2011). Because SF galaxies become less dusty at higher redshift and lower mass, a larger fraction of faint LAEs are observed towards higher redshift. The increase in the fraction of faint LAEs may contribute to the rapid increase in $\text{Ly}\alpha$ escape fraction from $z \sim 2$ to $z \sim 6$ (Konno et al. 2016).

6.2. Type 1 AGN UV LF and the Evolution

As mentioned in Section 4.4, our UV LFs of BL-LAEs are based on the total flux contributed from both the AGN and stellar components of host galaxies. Here we refer to the type 1 AGN UV LF as the UV LFs of BL-LAE with the flux contributed from the stellar components of galaxies removed. We derive the type 1 AGN UV LFs from UV LFs of BL-LAEs using the AGN UV flux ratio ($f_{\text{flux,AGN}}$) that is defined as the ratio of flux contributed from AGN to the total flux. Specifically, we calculate $f_{\text{flux,AGN}}$ of our BL-LAEs at each M_{UV} bin based on the results from Kakuma (2020). Kakuma (2020) obtained a sample of 37 type 1 AGN at $z = 2 - 3.5$ using the same method as mentioned in 3.2.2 and conducted SED fitting on their sample with the Code Investigating GALaxy Emission (CIGALE; Boquien et al. 2019). Their results are shown in Figure 15. Assuming a linear relation between M_{UV} and $\log f_{\text{flux,AGN}}$, we obtain the following best-fit model by MCMC:

$$\log f_{\text{UV,AGN}} = -3.056 M_{\text{UV}} - 0.118 \quad (22)$$

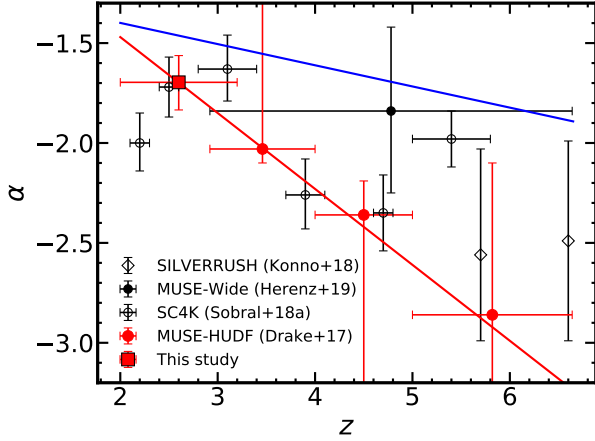


Figure 14. Evolution of the faint end slope of Ly α LF. Our result is denoted by the red square. The red circles, black filled circles, black open circles, and black open diamonds indicate the results from Drake et al. (2017), Herenz et al. (2019), Sobral et al. (2018a), and Konno et al. (2018), respectively. The error bars in the abscissa are the redshift ranges of the measurements. Our best-fit linear function is presented in the red line. The blue solid line shows the redshift evolution of the faint end slope of UV LF derived with photometrically selected galaxies (Parsa et al. 2016).

We multiply the M_{UV} of the UV LF in Figure 10 by

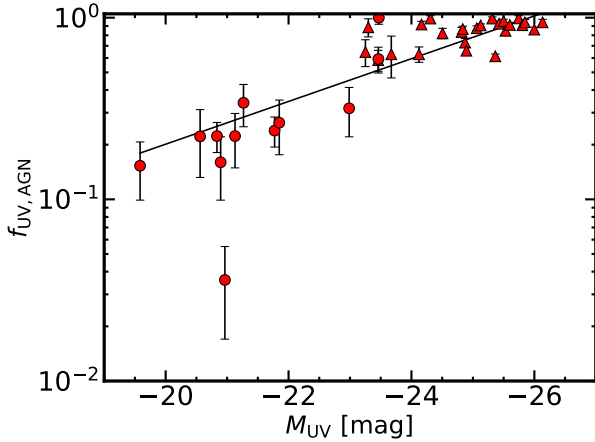


Figure 15. $M_{UV} - f_{UV,AGN}$ relation derived by Kakuma (2020). The red circles (triangles) indicate type 1 AGN selected from HETDEX (SDSS). Our best-fit linear function of $\log f_{UV,AGN} = -3.056M_{UV} - 0.118$ is shown in the black solid line (see text).

$f_{flux,AGN}$, obtaining the type 1 AGN UV LFs as shown in Figure 16. Our results reach the very faint end of UV absolute magnitude at $M_{UV} \sim -20$ and agree well with Bongiorno et al. (2007). Following the procedure

mentioned in Section 4.3, we fit our type 1 AGN UV LF with the DPL:

$$\phi_{AGN}(M_{UV})dM_{UV} = \frac{\phi_{AGN}^* dM_{UV}}{10^{(\alpha_{AGN}+1)(M_{UV}-M_{AGN}^*)} + 10^{(\beta_{AGN}+1)(M_{UV}-M_{AGN}^*)}}, \quad (23)$$

and obtain the best-fit parameters $\alpha_{AGN} = -1.26^{+0.10}_{-0.08}$, $\beta_{AGN} = -3.67^{+0.80}_{-1.13}$, $M_{AGN}^* = -25.44^{+0.50}_{-0.33}$, and $\log \phi_{AGN}^*[\text{Mpc}^{-3}] = -6.21^{+0.18}_{-0.16}$. Our best-fit AGN UV LF and the posterior distributions of the parameters are shown in Figure 16 and Figure 19, respectively. We compare our results with Ross et al. (2013) and Palanque-DeLabrouille et al. (2016), who studied the QSO UV LF using the pure luminosity evolution (PLE) model and the luminosity evolution and density evolution (LEDE) model. As presented in Figure 16, our type 1 AGN UV LF is consistent with the LEDE model of Ross et al. (2013) at $z = 2.75$, suggesting that the AGN UV LF evolve in both luminosities and number densities. We also compare our LFs at $z = 2 - 3$ with those at low redshifts, the type 1 AGN UV LF at $0.1 < z < 0.4$ (Kulkarni et al. 2019) and type 1 Seyfert UV LF at $0 < z < 0.15$ (Hao et al. 2005). In Figure 16, a strong evolution of type 1 AGN UV LFs is identified. At the bright end with $M_{UV} < -22$, we reproduce previous results that show the decrease of number density towards low redshift. At the faint end with $M_{UV} > -22$, our results show that the number density increases towards low redshift. Such a decrease (increase) of bright (faint) AGN number density towards low redshift can be interpreted as the AGN downsizing effect. First identified in X-ray studies (e.g., Hasinger 2008; Silverman et al. 2008), the AGN downsizing effect was observed in the UV LF only in the bright regime with $M_{UV} \lesssim -21$ (e.g., Hopkins et al. 2007; Croom et al. 2009; Ikeda et al. 2012). Our results further support the AGN downsizing effect for the very faint AGN with the absolute UV magnitude down to $M_{UV} \sim -20$.

The AGN downsizing effect may be connected with the quenching of massive galaxies that are observed in the local universe (e.g., Granato et al. 2004; Merloni 2004). Massive BHs, which reside in massive host-galaxies, grow at a high accretion rate and make up the bright end of the AGN UV LFs at $z \sim 2 - 3$. Towards lower redshift, the intense AGN activity in massive galaxies may gradually dispel gas from DM halos, resulting in the halt of star formation in the host galaxies as well as the decrease of BH accretion rate. The AGN become dimmer and populate the faint end of the UV LF. On the other hand, the moderate AGN feedback from less massive BHs would allow the host galaxies to

keep their gas, supplying fuel to both star formation and BH accretion (e.g., Babić et al. 2007; Hirschmann et al. 2014).

To further investigate the redshift evolution of Ly α and UV LFs within in $z \sim 2 - 3$, a larger sample of LAE is needed. These analyses will be presented in our future studies that incorporate forthcoming HETDEX data release.

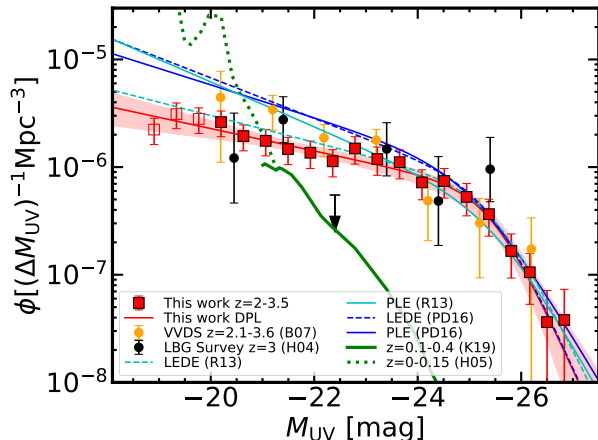


Figure 16. Type 1 AGN UV LF. Our results at $z = 2 - 3.5$ are presented in the red squares. Similar to Figure 10, data points that may be affected by incompleteness are marked with open red squares. The yellow circles denote the AGN UV LF from VVDS survey (Bongiorno et al. 2007; B07) at $z = 2.0 - 3.5$. The black circles indicate the AGN UV LF from LBG survey (Hunt et al. 2004; H04) at $z \sim 3$. The cyan and blue lines are the predicted QSO UV LF at $z = 2.75$ from Ross et al. (2013, R13) and Palanque-Delabrouille et al. (2016, PD16), respectively, based on the PLE (solid) and LEDE (dashed) models. The green dashed and solid lines represent the UF LF of type 1 Seyfert galaxies at $0 < z < 0.15$ (Hao et al. 2005, H05) and the type 1 AGN UV LF at $0.1 < z < 0.4$ (Kulkarni et al. 2019, K19), respectively.

7. SUMMARY

We investigate the Ly α and UV LFs of LAEs at $z = 2 - 3.5$ that are obtained from the HETDEX spectroscopic survey. Our LAE sample include 16194 SF galaxies and 2126 type 1 AGN with $EW_0 > 20 \text{ \AA}$ that are spectroscopically identified in a sky area of 11.4 deg^2 . Our main results are summarized below.

We derive the Ly α LF of LAEs at $z = 2 - 3.5$ in the Ly α luminosity range of $43.3 < \log L_{\text{Ly}\alpha} [\text{erg s}^{-1}] < 45.5$. Our Ly α LF is consistent with those from previous studies. At $\log L_{\text{Ly}\alpha} [\text{erg s}^{-1}] > 43.5$, our Ly α LF shows a clear bright-end hump. This is the first confirmation of such a bright-end hump with spectroscopically identified LAE samples. We confirm that the bright-end hump

can be fully explained by type 1 AGN, which has been suggested in previous studies (e.g., Konno et al. 2016; Matthee et al. 2017; Sobral et al. 2018a; Calhau et al. 2020; Spinoso et al. 2020).

Combining our Ly α LF with the one derived by Casata et al. (2011), we show that the Ly α LF at $z \sim 2 - 3$ can be fitted with the combination of the Schechter function and the double power law. Our Ly α LF provides strong constraints at the bright end, reducing the degeneracy of the faint end slope α_{Sch} and L_{Sch}^* by allowing all three Schechter parameters to be fitted simultaneously. From the Schechter component of our Ly α LF, we measure the faint end slope to be $\alpha_{\text{Sch}} = -1.70^{+0.13}_{-0.14}$ at $z = 2 - 3.2$. We investigate the redshift evolution of α_{Sch} based on our measurement and those from previous studies. We find that there is a possible redshift evolution of α_{Sch} over $z \sim 2 - 6$ with a correlation coefficient $r = -0.72$ at the confidence level of 85%. We obtain a linear relation $\alpha_{\text{Sch}} = -0.38^{+0.18}_{-0.26} z - 0.71^{+0.86}_{-0.60}$ at $z \sim 2 - 6$. Comparing with the linear relation of α_{Sch} of the UV LF, we find α_{Sch} of the Ly α LF may decrease more rapidly towards high redshift.

We derive the UV LF of LAEs at $z = 2 - 3.5$ in the range of $-27 < M_{\text{UV}} < 20$, connecting the SF galaxy and AGN regimes. Our UV LF are consistent with previous results of QSO UV LF at $M_{\text{UV}} < -23$ and LAE UV LF at $M_{\text{UV}} > -21.5$. Combining our results and the UV LF of galaxies at $z \sim 3$, we calculate the LAE number fraction as a function of M_{UV} . Combining with previous measurements, we show that at M_{UV} fainter (brighter) than $M_{\text{UV}}^* \sim -21$, X_{LAE} decreases (increases) with M_{UV} .

We derive the type 1 AGN UV LF based on the UV LF of LAEs. Our type 1 AGN UV LF reaches a very faint absolute UV magnitude of $M_{\text{UV}} \sim -20$ and agrees well with those from previous studies at similar redshift. Comparing with the results at lower redshifts, we find that the number density of faint ($M_{\text{UV}} > -21$) AGN increases from $z \sim 2$ to $z \sim 0$. Such a number density evolution is compatible with AGN downsizing effect, which may have a close connection with the quenching of galaxy formation.

ACKNOWLEDGMENTS

We thank the anonymous reviewer for the constructive comments that improve the quality of this work. YZ thanks E. Komatsu for his help during the completion of this work. SLF acknowledges support from the National Science Foundation through award AST-1908817. CMC thanks the National Science Foundation for support through grants AST-1814034 and AST-2009577, the University of Texas at Austin College of Natural Sciences, and the Research Corporation for Science Advancement from a 2019 Cottrell Scholar Award sponsored by IF/THEN, an initiative of Lyda Hill Philanthropies.

HETDEX is led by the University of Texas at Austin McDonald Observatory and Department of Astronomy with participation from the Ludwig-Maximilians-Universität München, Max-Planck-Institut für Extraterrestrische Physik (MPE), Leibniz-Institut für Astrophysik Potsdam (AIP), Texas A&M University, Pennsylvania State University, Institut für Astrophysik Göttingen, The University of Oxford, Max-Planck-Institut für Astrophysik (MPA), The University of Tokyo and Missouri University of Science and Technology. In addition to Institutional support, HETDEX is funded by the National Science Foundation (grant AST-0926815), the State of Texas, the US Air Force (AFRL FA9451-04-2-0355), and generous support from private individuals and foundations. The observations were obtained with the Hobby-Eberly Telescope (HET), which is a joint project of the University of Texas at Austin, the Pennsylvania State University, Ludwig-Maximilians-Universität München, and Georg-August-Universität Göttingen. The HET is named in honor of its principal benefactors, William P. Hobby and Robert E. Eberly. VIRUS is a joint project of the University of Texas at Austin, Leibniz-Institut für Astrophysik Potsdam (AIP), Texas A&M University, Max-Planck-Institut für Extraterrestrische Physik (MPE), Ludwig-Maximilians-Universität München, The University of Oxford, Pennsylvania State University, Institut für Astrophysik Göttingen, Max-Planck-Institut für Astro-

physik (MPA) The Texas Advanced Computing Center (TACC) at The University of Texas at Austin provided high performance computing, visualization, and storage resources that contributed to the research results reported within this paper.

The Institute for Gravitation and the Cosmos is supported by the Eberly College of Science and the Office of the Senior Vice President for Research at The Pennsylvania State University.

The Hyper Suprime-Cam (HSC) collaboration includes the astronomical communities of Japan and Taiwan, and Princeton University. The HSC instrumentation and software were developed by the National Astronomical Observatory of Japan (NAOJ), the Kavli Institute for the Physics and Mathematics of the Universe (Kavli IPMU), the University of Tokyo, the High Energy Accelerator Research Organization (KEK), the Academia Sinica Institute for Astronomy and Astrophysics in Taiwan (ASIAA), and Princeton University. Funding was contributed by the FIRST program from the Japanese Cabinet Office, the Ministry of Education, Culture, Sports, Science and Technology (MEXT), the Japan Society for the Promotion of Science (JSPS), Japan Science and Technology Agency (JST), the Toray Science Foundation, NAOJ, Kavli IPMU, KEK, ASIAA, and Princeton University.

This paper makes use of software developed for the Large Synoptic Survey Telescope. We thank the LSST Project for making their code available as free software at <http://dm.lsst.org>.

This research is based in part on data collected at Subaru Telescope, which is operated by the National Astronomical Observatory of Japan. We are honored and grateful for the opportunity of observing the Universe from Maunakea, which has the cultural, historical and natural significance in Hawaii.

This paper is supported by World Premier International Research Center Initiative (WPI Initiative), MEXT, Japan, and KAKENHI Grant-in-Aid for Scientific Research (A) (19H00697, 20H00180, and 21H04467) through the Japan Society for the Promotion of Science (JSPS).

REFERENCES

- Aihara, H., Arimoto, N., Armstrong, R., et al. 2018, PASJ, 70, S4, doi: [10.1093/pasj/psx066](https://doi.org/10.1093/pasj/psx066)
- Aihara, H., AlSayyad, Y., Ando, M., et al. 2019, PASJ, 71, 114, doi: [10.1093/pasj/psz103](https://doi.org/10.1093/pasj/psz103)
- Ando, M., Ohta, K., Iwata, I., et al. 2006, ApJL, 645, L9, doi: [10.1086/505652](https://doi.org/10.1086/505652)
- Babić, A., Miller, L., Jarvis, M. J., et al. 2007, A&A, 474, 755, doi: [10.1051/0004-6361:20078286](https://doi.org/10.1051/0004-6361:20078286)
- Blanc, G. A., Adams, J. J., Gebhardt, K., et al. 2011, ApJ, 736, 31, doi: [10.1088/0004-637X/736/1/31](https://doi.org/10.1088/0004-637X/736/1/31)
- Bongiorno, A., Zamorani, G., Gavignaud, I., et al. 2007, A&A, 472, 443, doi: [10.1051/0004-6361:20077611](https://doi.org/10.1051/0004-6361:20077611)

- Boquien, M., Burgarella, D., Roehly, Y., et al. 2019, *A&A*, 622, A103, doi: [10.1051/0004-6361/201834156](https://doi.org/10.1051/0004-6361/201834156)
- Bosch, J., Armstrong, R., Bickerton, S., et al. 2018, *PASJ*, 70, S5, doi: [10.1093/pasj/psx080](https://doi.org/10.1093/pasj/psx080)
- Bouwens, R. J., Illingworth, G. D., Oesch, P. A., et al. 2015, *ApJ*, 803, 34, doi: [10.1088/0004-637X/803/1/34](https://doi.org/10.1088/0004-637X/803/1/34)
- Boyle, B. J., Shanks, T., Croom, S. M., et al. 2000, *MNRAS*, 317, 1014, doi: [10.1046/j.1365-8711.2000.03730.x](https://doi.org/10.1046/j.1365-8711.2000.03730.x)
- Boyle, B. J., Shanks, T., & Peterson, B. A. 1988, *MNRAS*, 235, 935, doi: [10.1093/mnras/235.3.935](https://doi.org/10.1093/mnras/235.3.935)
- Calhau, J., Sobral, D., Santos, S., et al. 2020, *MNRAS*, 493, 3341, doi: [10.1093/mnras/staa476](https://doi.org/10.1093/mnras/staa476)
- Cassata, P., Le Fèvre, O., Garilli, B., et al. 2011, *A&A*, 525, A143, doi: [10.1051/0004-6361/201014410](https://doi.org/10.1051/0004-6361/201014410)
- Croom, S. M., Richards, G. T., Shanks, T., et al. 2009, *MNRAS*, 399, 1755, doi: [10.1111/j.1365-2966.2009.15398.x](https://doi.org/10.1111/j.1365-2966.2009.15398.x)
- Davis, M., Faber, S. M., Newman, J., et al. 2003, *Society of Photo-Optical Instrumentation Engineers (SPIE) Conference Series*, Vol. 4834, *Science Objectives and Early Results of the DEEP2 Redshift Survey*, ed. P. Guhathakurta, 161–172
- Dawson, S., Rhoads, J. E., Malhotra, S., et al. 2004, *ApJ*, 617, 707, doi: [10.1086/425572](https://doi.org/10.1086/425572)
- Deharveng, J.-M., Small, T., Barlow, T. A., et al. 2008, *ApJ*, 680, 1072, doi: [10.1086/587953](https://doi.org/10.1086/587953)
- Dijkstra, M., Haiman, Z., & Spaans, M. 2006, *ApJ*, 649, 14, doi: [10.1086/506243](https://doi.org/10.1086/506243)
- Drake, A. B., Garel, T., Wisotzki, L., et al. 2017, *A&A*, 608, A6, doi: [10.1051/0004-6361/201731431](https://doi.org/10.1051/0004-6361/201731431)
- Eddington, A. S. 1913, *MNRAS*, 73, 359, doi: [10.1093/mnras/73.5.359](https://doi.org/10.1093/mnras/73.5.359)
- Fabian, A. C. 2012, *ARA&A*, 50, 455, doi: [10.1146/annurev-astro-081811-125521](https://doi.org/10.1146/annurev-astro-081811-125521)
- Farrow, D. J., Sánchez, A. G., Ciardullo, R., et al. 2021, *arXiv e-prints*, arXiv:2104.04613, <https://arxiv.org/abs/2104.04613>
- Felten, J. E. 1976, *ApJ*, 207, 700, doi: [10.1086/154538](https://doi.org/10.1086/154538)
- Finkelstein, S. L., Rhoads, J. E., Malhotra, S., & Grogin, N. 2009, *ApJ*, 691, 465, doi: [10.1088/0004-637X/691/1/465](https://doi.org/10.1088/0004-637X/691/1/465)
- Finkelstein, S. L., Rhoads, J. E., Malhotra, S., Grogin, N., & Wang, J. 2008, *ApJ*, 678, 655, doi: [10.1086/525272](https://doi.org/10.1086/525272)
- Finkelstein, S. L., Rhoads, J. E., Malhotra, S., Pirzkal, N., & Wang, J. 2007, *ApJ*, 660, 1023, doi: [10.1086/513462](https://doi.org/10.1086/513462)
- Finkelstein, S. L., Ryan, Russell E., J., Papovich, C., et al. 2015, *ApJ*, 810, 71, doi: [10.1088/0004-637X/810/1/71](https://doi.org/10.1088/0004-637X/810/1/71)
- Foreman-Mackey, D., Hogg, D. W., Lang, D., & Goodman, J. 2013, *PASP*, 125, 306, doi: [10.1086/670067](https://doi.org/10.1086/670067)
- Gawiser, E., van Dokkum, P. G., Gronwall, C., et al. 2006, *ApJL*, 642, L13, doi: [10.1086/504467](https://doi.org/10.1086/504467)
- Granato, G. L., De Zotti, G., Silva, L., Bressan, A., & Danese, L. 2004, *ApJ*, 600, 580, doi: [10.1086/379875](https://doi.org/10.1086/379875)
- Gronke, M., Dijkstra, M., Trenti, M., & Wyithe, S. 2015, *MNRAS*, 449, 1284, doi: [10.1093/mnras/stv329](https://doi.org/10.1093/mnras/stv329)
- Gronwall, C., Ciardullo, R., Hickey, T., et al. 2007, *ApJ*, 667, 79, doi: [10.1086/520324](https://doi.org/10.1086/520324)
- Hao, L., Strauss, M. A., Fan, X., et al. 2005, *AJ*, 129, 1795, doi: [10.1086/428486](https://doi.org/10.1086/428486)
- Harikane, Y., Ouchi, M., Shibuya, T., et al. 2018, *ApJ*, 859, 84, doi: [10.3847/1538-4357/aabd80](https://doi.org/10.3847/1538-4357/aabd80)
- Hasinger, G. 2008, *A&A*, 490, 905, doi: [10.1051/0004-6361:200809839](https://doi.org/10.1051/0004-6361:200809839)
- Hayes, M., Schaerer, D., Östlin, G., et al. 2011, *ApJ*, 730, 8, doi: [10.1088/0004-637X/730/1/8](https://doi.org/10.1088/0004-637X/730/1/8)
- Herenz, E. C., Wisotzki, L., Saust, R., et al. 2019, *A&A*, 621, A107, doi: [10.1051/0004-6361/201834164](https://doi.org/10.1051/0004-6361/201834164)
- Hill, G. J. 2014, *Advanced Optical Technologies*, 3, 265, doi: [10.1515/aot-2014-0019](https://doi.org/10.1515/aot-2014-0019)
- Hill, G. J., Gebhardt, K., Komatsu, E., et al. 2008, *Astronomical Society of the Pacific Conference Series*, Vol. 399, *The Hobby-Eberly Telescope Dark Energy Experiment (HETDEX): Description and Early Pilot Survey Results*, ed. T. Kodama, T. Yamada, & K. Aoki, 115
- Hill, G. J., Kelz, A., Lee, H., et al. 2018a, in *Society of Photo-Optical Instrumentation Engineers (SPIE) Conference Series*, Vol. 10702, *Proc. SPIE*, 107021K
- Hill, G. J., Drory, N., Good, J. M., et al. 2018b, in *Society of Photo-Optical Instrumentation Engineers (SPIE) Conference Series*, Vol. 10700, *Ground-based and Airborne Telescopes VII*, ed. H. K. Marshall & J. Spyromilio, 107000P
- Hirschmann, M., Dolag, K., Saro, A., et al. 2014, *MNRAS*, 442, 2304, doi: [10.1093/mnras/stu1023](https://doi.org/10.1093/mnras/stu1023)
- Hopkins, P. F., Richards, G. T., & Hernquist, L. 2007, *ApJ*, 654, 731, doi: [10.1086/509629](https://doi.org/10.1086/509629)
- Hu, E. M., Cowie, L. L., Barger, A. J., et al. 2010, *ApJ*, 725, 394, doi: [10.1088/0004-637X/725/1/394](https://doi.org/10.1088/0004-637X/725/1/394)
- Hunt, M. P., Steidel, C. C., Adelberger, K. L., & Shapley, A. E. 2004, *ApJ*, 605, 625, doi: [10.1086/381727](https://doi.org/10.1086/381727)
- Ikeda, H., Nagao, T., Matsuoka, K., et al. 2012, *ApJ*, 756, 160, doi: [10.1088/0004-637X/756/2/160](https://doi.org/10.1088/0004-637X/756/2/160)
- Itoh, R., Ouchi, M., Zhang, H., et al. 2018, *ApJ*, 867, 46, doi: [10.3847/1538-4357/aadfe4](https://doi.org/10.3847/1538-4357/aadfe4)
- Kakuma, R. 2020, Master's thesis, The University of Tokyo, Tokyo, Japan
- Kashikawa, N., Shimasaku, K., Malkan, M. A., et al. 2006, *ApJ*, 648, 7, doi: [10.1086/504966](https://doi.org/10.1086/504966)

- Kashikawa, N., Nagao, T., Toshikawa, J., et al. 2012, *ApJ*, 761, 85, doi: [10.1088/0004-637X/761/2/85](https://doi.org/10.1088/0004-637X/761/2/85)
- Kelz, A., Jahn, T., Haynes, D., et al. 2014, *Society of Photo-Optical Instrumentation Engineers (SPIE) Conference Series*, Vol. 9147, VIRUS: assembly, testing and performance of 33,000 fibres for HETDEX, 914775
- Kim, Y., Im, M., Jeon, Y., et al. 2018, *ApJ*, 855, 138, doi: [10.3847/1538-4357/aaadae](https://doi.org/10.3847/1538-4357/aaadae)
- Koekemoer, A. M., Aussel, H., Calzetti, D., et al. 2007, *ApJS*, 172, 196, doi: [10.1086/520086](https://doi.org/10.1086/520086)
- Konno, A., Ouchi, M., Nakajima, K., et al. 2016, *ApJ*, 823, 20, doi: [10.3847/0004-637X/823/1/20](https://doi.org/10.3847/0004-637X/823/1/20)
- Konno, A., Ouchi, M., Shibuya, T., et al. 2018, *PASJ*, 70, S16, doi: [10.1093/pasj/psx131](https://doi.org/10.1093/pasj/psx131)
- Kriek, M., Shapley, A. E., Reddy, N. A., et al. 2015, *ApJS*, 218, 15, doi: [10.1088/0067-0049/218/2/15](https://doi.org/10.1088/0067-0049/218/2/15)
- Kulkarni, G., Worseck, G., & Hennawi, J. F. 2019, *MNRAS*, 488, 1035, doi: [10.1093/mnras/stz1493](https://doi.org/10.1093/mnras/stz1493)
- Kusakabe, H., Blaizot, J., Garel, T., et al. 2020, *A&A*, 638, A12, doi: [10.1051/0004-6361/201937340](https://doi.org/10.1051/0004-6361/201937340)
- Laigle, C., McCracken, H. J., Ilbert, O., et al. 2016, *ApJS*, 224, 24, doi: [10.3847/0067-0049/224/2/24](https://doi.org/10.3847/0067-0049/224/2/24)
- Leung, A. S., Acquaviva, V., Gawiser, E., et al. 2017, *ApJ*, 843, 130, doi: [10.3847/1538-4357/aa71af](https://doi.org/10.3847/1538-4357/aa71af)
- Lusso, E., Worseck, G., Hennawi, J. F., et al. 2015, *MNRAS*, 449, 4204, doi: [10.1093/mnras/stv516](https://doi.org/10.1093/mnras/stv516)
- Malhotra, S., & Rhoads, J. E. 2004, *ApJL*, 617, L5, doi: [10.1086/427182](https://doi.org/10.1086/427182)
- Massey, R., Stoughton, C., Leauthaud, A., et al. 2010, *MNRAS*, 401, 371, doi: [10.1111/j.1365-2966.2009.15638.x](https://doi.org/10.1111/j.1365-2966.2009.15638.x)
- Matthee, J., Sobral, D., Best, P., et al. 2017, *MNRAS*, 471, 629, doi: [10.1093/mnras/stx1569](https://doi.org/10.1093/mnras/stx1569)
- Matthee, J., Sobral, D., Gronke, M., et al. 2018, *A&A*, 619, A136, doi: [10.1051/0004-6361/201833528](https://doi.org/10.1051/0004-6361/201833528)
- Merloni, A. 2004, *MNRAS*, 353, 1035, doi: [10.1111/j.1365-2966.2004.08147.x](https://doi.org/10.1111/j.1365-2966.2004.08147.x)
- Merloni, A., & Heinz, S. 2013, *Evolution of Active Galactic Nuclei*, ed. T. D. Oswalt & W. C. Keel, Vol. 6, 503
- Moffat, A. F. J. 1969, *A&A*, 3, 455
- Nagao, T., Motohara, K., Maiolino, R., et al. 2005, *ApJL*, 631, L5, doi: [10.1086/497135](https://doi.org/10.1086/497135)
- Netzer, H. 1990, in *Act. Galact. Nucl.*, ed. R. Blandford, H. Netzer, L. Woltjer, T. L. Courvoisier, & M. Mayor, 57–160
- Oke, J. B. 1974, *ApJS*, 27, 21, doi: [10.1086/190287](https://doi.org/10.1086/190287)
- Ono, Y., Ouchi, M., Shimasaku, K., et al. 2010a, *ApJ*, 724, 1524, doi: [10.1088/0004-637X/724/2/1524](https://doi.org/10.1088/0004-637X/724/2/1524)
- . 2010b, *MNRAS*, 402, 1580, doi: [10.1111/j.1365-2966.2009.16034.x](https://doi.org/10.1111/j.1365-2966.2009.16034.x)
- Ouchi, M., Ono, Y., & Shibuya, T. 2020, *ARA&A*, 58, 617, doi: [10.1146/annurev-astro-032620-021859](https://doi.org/10.1146/annurev-astro-032620-021859)
- Ouchi, M., Shimasaku, K., Akiyama, M., et al. 2008, *ApJS*, 176, 301, doi: [10.1086/527673](https://doi.org/10.1086/527673)
- Ouchi, M., Shimasaku, K., Furusawa, H., et al. 2010, *ApJ*, 723, 869, doi: [10.1088/0004-637X/723/1/869](https://doi.org/10.1088/0004-637X/723/1/869)
- Palanque-Delabrouille, N., Magneville, C., Yèche, C., et al. 2016, *A&A*, 587, A41, doi: [10.1051/0004-6361/201527392](https://doi.org/10.1051/0004-6361/201527392)
- Pâris, I., Petitjean, P., Aubourg, É., et al. 2018, *A&A*, 613, A51, doi: [10.1051/0004-6361/201732445](https://doi.org/10.1051/0004-6361/201732445)
- Parsa, S., Dunlop, J. S., McLure, R. J., & Mortlock, A. 2016, *MNRAS*, 456, 3194, doi: [10.1093/mnras/stv2857](https://doi.org/10.1093/mnras/stv2857)
- Pei, Y. C. 1995, *ApJ*, 438, 623, doi: [10.1086/175105](https://doi.org/10.1086/175105)
- Pentericci, L., Grazian, A., Fontana, A., et al. 2009, *A&A*, 494, 553, doi: [10.1051/0004-6361:200810722](https://doi.org/10.1051/0004-6361:200810722)
- Rakshit, S., Stalin, C. S., & Kotilainen, J. 2020, *ApJS*, 249, 17, doi: [10.3847/1538-4365/ab99c5](https://doi.org/10.3847/1538-4365/ab99c5)
- Ramsey, L. W., Sebring, T. A., & Sneden, C. A. 1994, *Society of Photo-Optical Instrumentation Engineers (SPIE) Conference Series*, Vol. 2199, Spectroscopic survey telescope project, ed. L. M. Stepp, 31–40
- Rhoads, J. E., Malhotra, S., Dey, A., et al. 2000, *ApJL*, 545, L85, doi: [10.1086/317874](https://doi.org/10.1086/317874)
- Richards, G. T., Strauss, M. A., Fan, X., et al. 2006a, *AJ*, 131, 2766, doi: [10.1086/503559](https://doi.org/10.1086/503559)
- Richards, G. T., Lacy, M., Storrie-Lombardi, L. J., et al. 2006b, *ApJS*, 166, 470, doi: [10.1086/506525](https://doi.org/10.1086/506525)
- Ross, N. P., McGreer, I. D., White, M., et al. 2013, *ApJ*, 773, 14, doi: [10.1088/0004-637X/773/1/14](https://doi.org/10.1088/0004-637X/773/1/14)
- Sakai, N. 2021, Master's thesis, The University of Tokyo, Tokyo, Japan
- Schechter, P. 1976, *ApJ*, 203, 297, doi: [10.1086/154079](https://doi.org/10.1086/154079)
- Schmidt, M. 1968, *ApJ*, 151, 393, doi: [10.1086/149446](https://doi.org/10.1086/149446)
- Schwarz, G. 1978, *Annals of Statistics*, 6, 461
- Shen, Y., Richards, G. T., Strauss, M. A., et al. 2011, *ApJS*, 194, 45, doi: [10.1088/0067-0049/194/2/45](https://doi.org/10.1088/0067-0049/194/2/45)
- Silverman, J. D., Green, P. J., Barkhouse, W. A., et al. 2008, *ApJ*, 679, 118, doi: [10.1086/529572](https://doi.org/10.1086/529572)
- Sobral, D., Santos, S., Matthee, J., et al. 2018a, *MNRAS*, 476, 4725, doi: [10.1093/mnras/sty378](https://doi.org/10.1093/mnras/sty378)
- Sobral, D., Matthee, J., Best, P., et al. 2017, *MNRAS*, 466, 1242, doi: [10.1093/mnras/stw3090](https://doi.org/10.1093/mnras/stw3090)
- Sobral, D., Matthee, J., Darvish, B., et al. 2018b, *MNRAS*, 477, 2817, doi: [10.1093/mnras/sty782](https://doi.org/10.1093/mnras/sty782)
- Spinoso, D., Orsi, A., López-Sanjuan, C., et al. 2020, *arXiv e-prints*, arXiv:2006.15084, <https://arxiv.org/abs/2006.15084>
- Stark, D. P., Ellis, R. S., Chiu, K., Ouchi, M., & Bunker, A. 2010, *MNRAS*, 408, 1628, doi: [10.1111/j.1365-2966.2010.17227.x](https://doi.org/10.1111/j.1365-2966.2010.17227.x)

- Stevans, M. L., Finkelstein, S. L., Wold, I., et al. 2018, *ApJ*, 863, 63, doi: [10.3847/1538-4357/aacbd7](https://doi.org/10.3847/1538-4357/aacbd7)
- Tasca, L. A. M., Le Fèvre, O., Ribeiro, B., et al. 2017, *A&A*, 600, A110, doi: [10.1051/0004-6361/201527963](https://doi.org/10.1051/0004-6361/201527963)
- Tilvi, V., Malhotra, S., Rhoads, J. E., et al. 2020, *ApJL*, 891, L10, doi: [10.3847/2041-8213/ab75ec](https://doi.org/10.3847/2041-8213/ab75ec)
- Tody, D. 1986, in *Society of Photo-Optical Instrumentation Engineers (SPIE) Conference Series*, Vol. 627, *Instrumentation in astronomy VI*, ed. D. L. Crawford, 733
- Trujillo, I., Aguerri, J. A. L., Cepa, J., & Gutiérrez, C. M. 2001, *MNRAS*, 328, 977, doi: [10.1046/j.1365-8711.2001.04937.x](https://doi.org/10.1046/j.1365-8711.2001.04937.x)
- Verhamme, A., Garel, T., Ventou, E., et al. 2018, *MNRAS*, 478, L60, doi: [10.1093/mnras/sly058](https://doi.org/10.1093/mnras/sly058)
- Wold, I. G. B., Finkelstein, S. L., Barger, A. J., Cowie, L. L., & Rosenwasser, B. 2017, *ApJ*, 848, 108, doi: [10.3847/1538-4357/aa8d6b](https://doi.org/10.3847/1538-4357/aa8d6b)
- Zheng, Z.-Y., Finkelstein, S. L., Finkelstein, K., et al. 2013, *MNRAS*, 431, 3589, doi: [10.1093/mnras/stt440](https://doi.org/10.1093/mnras/stt440)
- Zheng, Z.-Y., Wang, J., Rhoads, J., et al. 2017, *ApJL*, 842, L22, doi: [10.3847/2041-8213/aa794f](https://doi.org/10.3847/2041-8213/aa794f)

APPENDIX

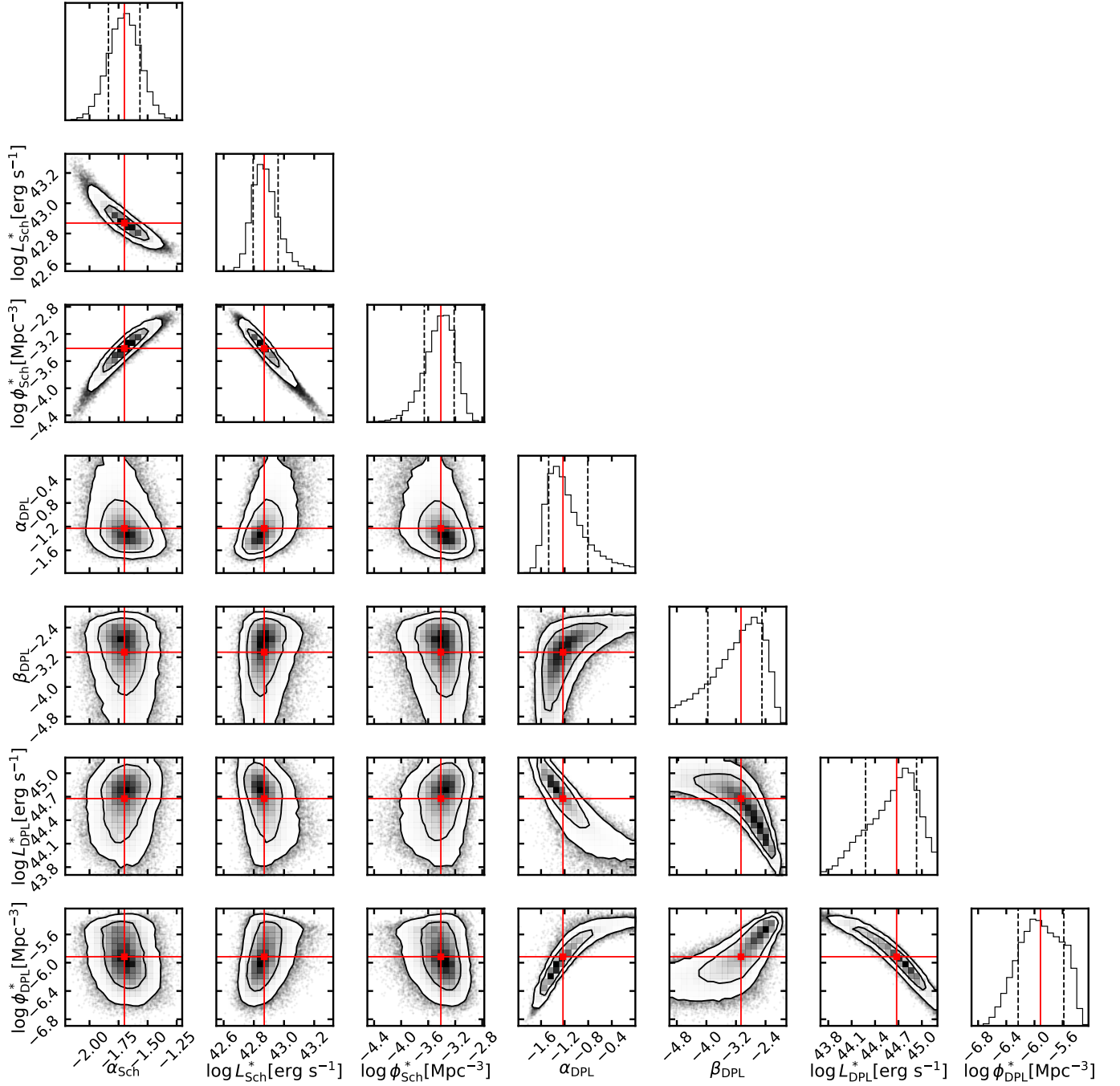


Figure 17. Error contours of our best-fit Ly α LF (Model 1). The red crosses denotes the best-fit results of the parameters. The inner (outer) contour indicates the 68.3% (95.4%) confidence level.

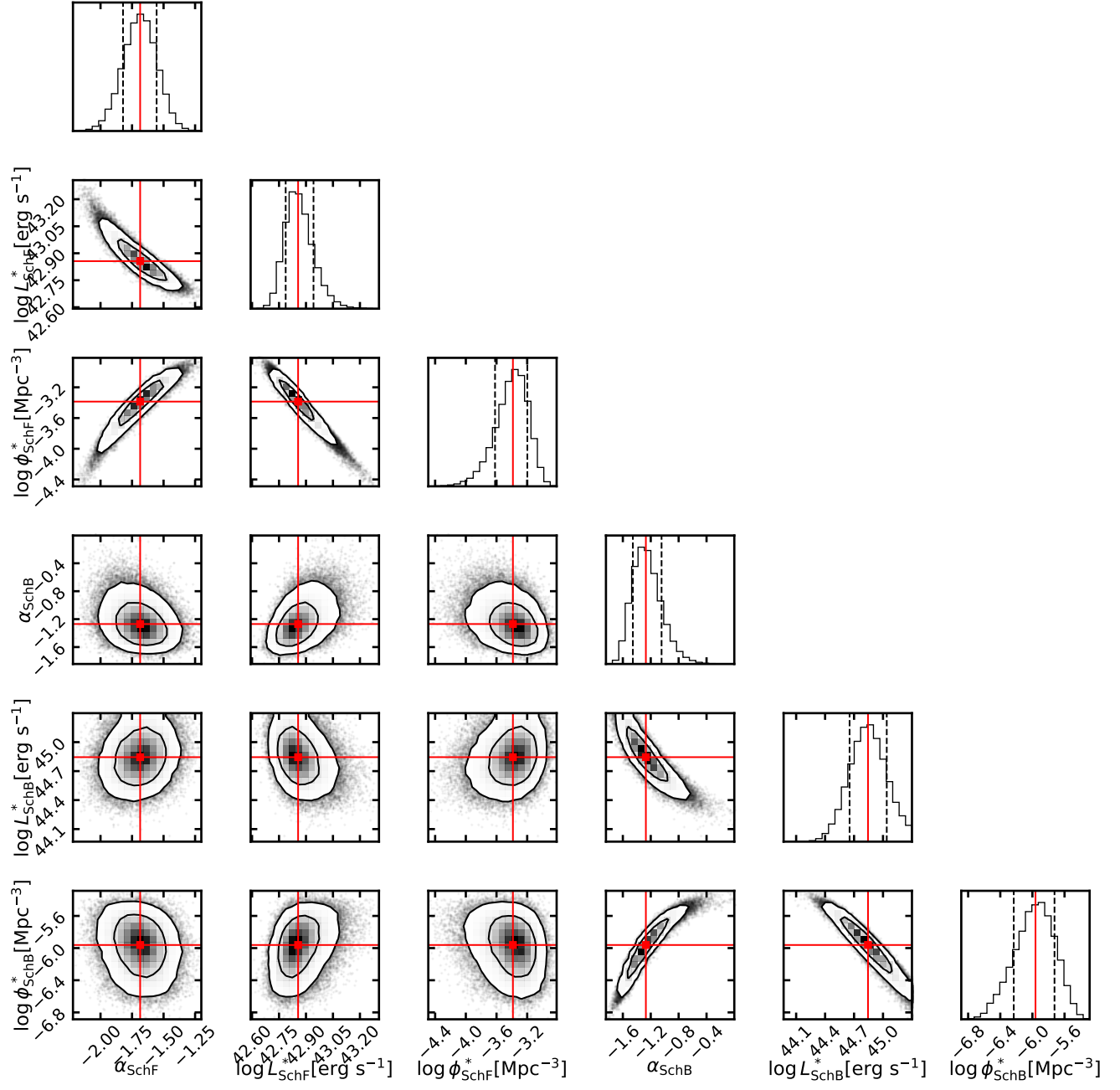


Figure 18. Same as Figure 17, but for Model 2. The Schechter parameters of the faint and bright component are denoted with subscripts of “SchF” and “SchB”, respectively.

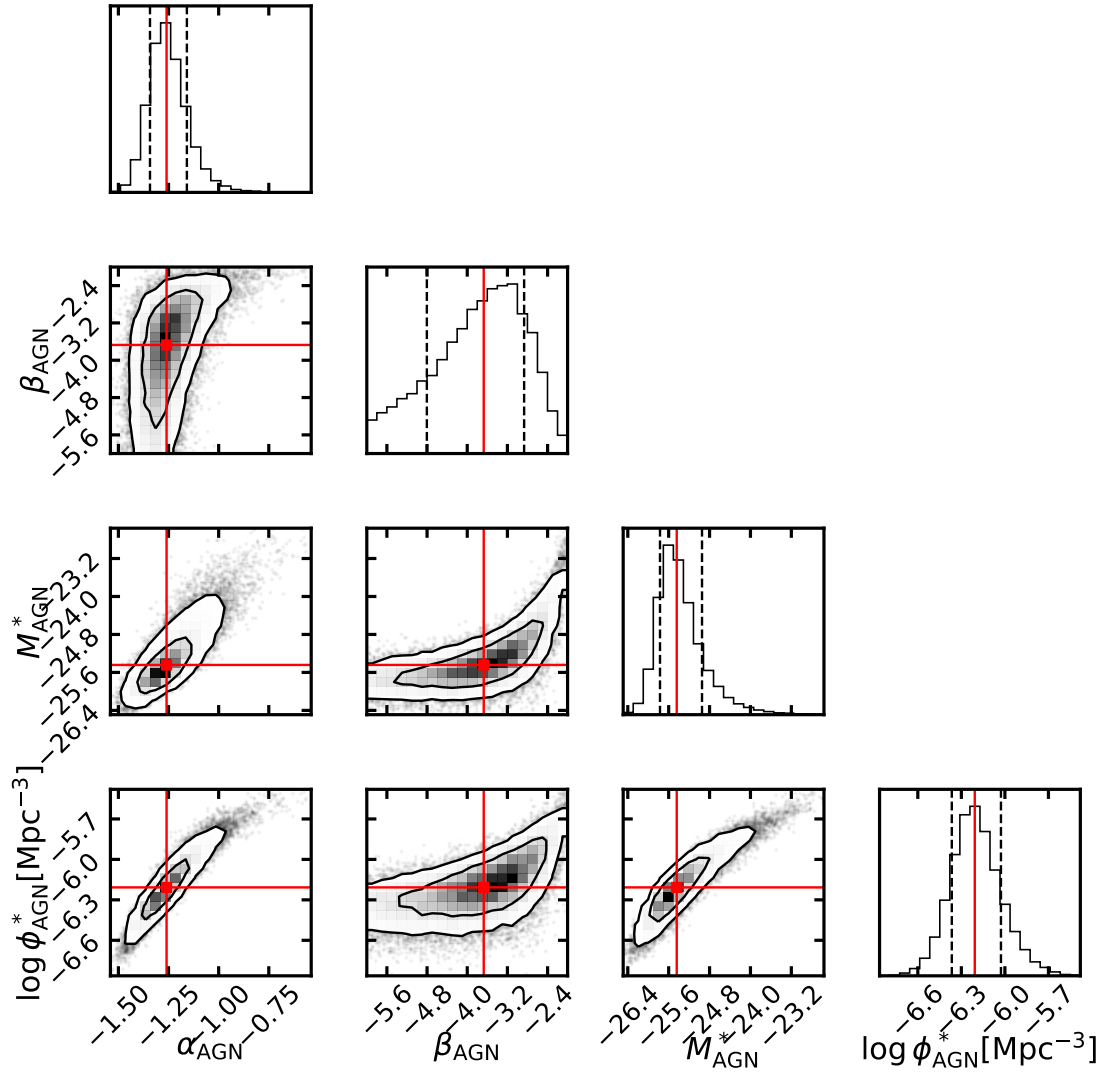


Figure 19. Same as Figure 17, but for type 1 AGN UV LF.